

Flexible Motor Sequence Generation during Stereotyped Escape Responses

Yuan Wang^{1,2,#}, Xiaoqian Zhang^{1,2,#}, Qi Xin^{1,2,#}, Wesley Hung^{3,4}, Jeremy Florman⁵,
Jing Huo^{1,2}, Tianqi Xu^{1,2}, Yu Xie¹, Mark J. Alkema⁵, Mei Zhen^{3,4}, Quan Wen^{1,2,6,*}

¹*Hefei National Laboratory for Physical Sciences at the Microscale, Center for Integrative
Imaging, School of Life Sciences, University of Science and Technology of China, Hefei, China*

²*Chinese Academy of Sciences Key Laboratory of Brain Function and Disease, Hefei, China*

³*Samuel Lunenfeld Research Institute, Mount Sinai Hospital, Toronto, ON, Canada M5G 1X5;*

⁴*University of Toronto, Toronto, ON, Canada M5S 1A8*

⁵*Department of Neurobiology, University of Massachusetts Medical School, 364 Plantation 8
Street, Worcester, MA 01605, USA*

⁶*Center for Excellence in Brain Science and Intelligence Technology, Chinese Academy of
Sciences, Shanghai, China*

[#]These authors contribute equally to this work

*Corresponding author: qwen@ustc.edu.cn

Abstract

Complex animal behaviors arise from a flexible combination of stereotyped motor primitives. Here we use the escape responses of the nematode *Caenorhabditis elegans* to study how a nervous system dynamically explores the action space. The initiation of the escape responses is predictable: the animal moves away from a potential threat, a mechanical or thermal stimulus. But the motor sequence and the timing that follow are variable. We report that a feedforward excitation between neurons encoding distinct motor states underlies robust motor sequence generation, while mutual inhibition between these neurons controls the flexibility of timing in a motor sequence. Electrical synapses contribute to feedforward coupling whereas glutamatergic synapses contribute to inhibition. We conclude that *C. elegans* generates robust and flexible motor sequences by combining an excitatory coupling and a winner-take-all operation via mutual inhibition between motor modules.

Keywords

Motor sequence generation, feedforward excitation, mutual inhibition, winner-take-all, escape response

Introduction

Nervous systems transform sensation into a sequence of actions. The motor repertoire, constrained by the biomechanics of gait, comprises a finite number of motor primitives that are stereotyped across individuals (Berman, Choi, Bialek, & Shaevitz, 2014; M. Liu, Sharma, Shaevitz, & Leifer, 2018; Stephens, Johnson-Kerner, Bialek, & Ryu, 2008). On the other hand, behavioral flexibility allows an animal to explore the action space, to select better strategies for acquiring reward or avoiding danger in a changing environment (Sutton & Barto, 2017).

Many factors contribute to behavioral flexibility (Dhawale, Smith, & Olveczky, 2017; Gordus, Pokala, Levy, Flavell, & Bargmann, 2015; Remington, Egger, Narain, Wang, & Jazayeri, 2018). Actions may be generated by an inherently noisy system: synapses are unreliable (Allen & Stevens, 1994), neurons generate variable spike trains (Mainen & Sejnowski, 1995), and neural circuits may operate near the edge of chaos (van Vreeswijk & Sompolinsky, 1996). On the other hand, neural networks, whether adaptive or hard-wired, have structures that shape population neural dynamics onto a low dimensional manifold, where nonrandom and ordered activity patterns emerge (Ganguli et al., 2008; Harvey, Coen, & Tank, 2012; Inagaki, Inagaki, Romani, & Svoboda, 2018). Computational models have promised to provide a unified view of these observations (Burak & Fiete, 2012; Mastrogiuseppe & Ostojic, 2018; Roberts et al., 2016), but a deep connection between theories and experiments remains to be established.

The initiation of escape responses of the nematode *Caenorhabditis elegans* (*C. elegans*) has long been viewed as an instinctive reflex. Upon a gentle touch to its anterior body, the ventral cord-projecting premotor interneurons AVA/AVD/AVE relay mechanosensory inputs to motor neurons and reliably drive a backward movement (Chalfie et al., 1985; Pirri, McPherson, Donnelly,

Francis, & Alkema, 2009; Wicks, Roehrig, & Rankin, 1996). While *C. elegans* stays committed to its escape decision, the animal remains flexible in its approach to complete the motor sequence. After the reversal, the animal may or may not reorient its body via a deep omega (Ω) turn, before moving forward (**Figure 1A**). This allows the animal to resume forward movement in either the original or a new direction. Notably, which action to select and when to execute exhibit trial to trial variability, and they can be coupled. For example, a previous study (Gray, Hill, & Bargmann, 2005) has shown that a longer reversal is likely to be followed by an omega turn.

We sought to understand algorithms and circuit mechanisms for motor sequence generation by investigating recurrently connected interneurons, which are positioned between sensory and motor neurons in the *C. elegans* nervous system (**Figure 2—figure supplement 1A**). Previous studies on this layer of neural network (**Figure 2—figure supplement 1A**) have implicated their roles in exploratory behaviors (Gray et al., 2005; Iino & Yoshida, 2009; Mori & Ohshima, 1995; Pierce-Shimomura, Morse, & Lockery, 1999). During navigation, *C. elegans* moves towards a new direction by making a reversal and/or a turn in a probabilistic manner. Cell ablation studies revealed that the frequencies of reversals or turns were differentially modulated by many local interneurons including AIB and RIB (Gray et al., 2005). Here we ask whether and how activities of local interneurons and their synaptic interactions shape the dynamics of a motor sequence during escape responses.

Several models have been proposed to account for motor sequence generation. In a class of synaptic chain models (Abeles, 1991; Long, Jin, & Fee, 2010), feedforward excitation between transiently activated groups of neurons controls the timing of actions hierarchically. Sequential neural activity may also emerge from a cooperation between external inputs and local synaptic interactions in a recurrent network (Rajan, Harvey, & Tank, 2016; Seeds et al., 2014). We find that

77 neurons encoding distinct motor states, such as reversal and omega turn, use electrical coupling to
78 reliably drive motor state transitions, whereas they exploit mutual inhibition to flexibly control the
79 timing of an action in a sequence. Our findings provide new insights into how the nervous system
80 organizes time-ordered and variable motor activities, by which stereotyped and flexible animal
81 behaviors emerge.

Results

Stereotypical and flexible motor patterns constitute *C. elegans* escape responses

A potentially threatening sensory stimulus will trigger an animal's escape response. For example, a gentle touch on the *C. elegans* head, which activates specific mechanosensory neurons ALM/AVM (Chalfie et al., 1985), can induce a reversal or an omega turn (**Figure 1A** and **Video 1**).

We quantitatively characterized the escape responses from animals in which channelrhodopsin (ChR2) was expressed in ALM/AVM neurons (*Pmec-4::ChR2; lite-1*), and optogenetic stimulation was given to the same sensory neurons at a defined light intensity and pulse duration during forward movement (see Materials and Methods) (Leifer, Fang-Yen, Gershow, Alkema, & Samuel, 2011). ALM/AVM-triggered backward movements responses were robust (only ~ 10% trials did not respond, **Figure 1C** left), but subsequent motor sequences constituting each trial varied. Animals exhibited two main types of motor patterns: (1) backward movement was followed by a deep omega turn, and the animal moved forward in a new direction that was different from that before stimulation; (2) an animal executed backward movement and then resumed forward movement in a similar direction as that before stimulation (**Figure 1A** and **Video 1**). The head and the tail were diametrically opposed to each other in (1); whereas they were likely aligned to each other in (2) (**Figure 1—figure supplement 1A**). Occasionally, an animal paused (1/674 trials) before resuming forward movement (**Figure 1A**), which can be regarded as the third motor pattern.

The reversal length distribution is broad (*Figure 1C* left) and bimodal (*Figure 1—figure supplement 1B*). This observation motivated us to describe behavior statistics by introducing two types of transitions and the corresponding transition rates $r(t)$. Among all reversals survived to time t , $r(t)\Delta t$ computes the fraction of events that will make a transition to another motor state within the time bin Δt . The type-I (RF) transition rate, r_1 , determines the transition probability from reversal to forward movement; the type-II (RT) transition rate, r_2 , determines the transition probability from reversal to omega turn (*Figure 1B* and Materials and Methods). $r_1(t)$ rapidly plateaued in about one second, while $r_2(t)$ increased and gradually became the dominant mode (*Figure 1C* right). The escape responses induced by a focused infrared laser light (Mohammadi, Byrne Rodgers, Kotera, & Ryu, 2013) exhibited qualitatively similar statistics to ALM/AVM-triggered responses (*Figure 1D*).

This quantification, which was consistent with a previous observation and description for spontaneous reversals during exploratory behaviors (Gray et al., 2005), confirms the notion that the longer a reversal, the more likely the reversal is followed by a turn.

Local interneurons in the backward module modulate motor state transitions

We ask how neural dynamics underlie the behavioral variation. Whole brain and multi-neuron calcium imaging of fixed and behaving animals suggested that population interneuron activities, which perform sensorimotor transformation, encode distinct motor states (Gordus et al., 2015; Kato et al., 2015; Kawano et al., 2011; Li, Liu, Zheng, & Xu, 2014; Luo et al., 2014; Nguyen et al., 2016; Roberts et al., 2016; Venkatachalam et al., 2016) (*Figure 2A* and *Figure 2—figure*

supplement 1B). Several interneurons, including the ventral cord-projecting premotor interneurons AVA and AVE, and the local interneurons AIB and RIM, exhibited increased calcium activity during backward movements (Kato et al., 2015; Laurent et al., 2015; Luo et al., 2014) (*Figure 2A* and *Figure 2—figure supplement 1B*).

Structural and functional studies of AIB (Gray et al., 2005; White, Southgate, Thomson, & Brenner, 1986) indicate that they may play important roles in motor state transitions (*Figure 2A*). First, AIB establish recurrent connections with the premotor interneurons AVA and AVE that potentiate backward movement either directly through chemical synapses or indirectly through electrical and chemical connections with RIM (*Figure 2A*). Second, AIB form gap junctions with the inter/motor neurons RIV (White et al., 1986), which play a role in generating a ventral-biased turning behavior (*Figure 2A*) (Gray et al., 2005). Third, AIB exhibit ramping calcium activity during reversals (Kato et al., 2015; Laurent et al., 2015; Luo et al., 2014), and finally, laser ablation of AIB significantly reduces the frequency of reversals during food search behavior (Gray et al., 2005).

We first examined neuronal correlate of behavioral flexibility in action selection. We compared the AIB ramping activity (*Pinx-I::GCaMP6*; *Pinx-I::wCherry*) in different action sequences during either spontaneous or thermal-stimulus-triggered behaviors (*Figure 2B-C* and *Figure 2—figure supplement 1B-C*). If the fluorescence signal ($\Delta R(t)/R_0$) reflects a change of intracellular free calcium concentration $[Ca^{2+}]$, the ramping rate, defined as $\zeta = \frac{dR}{dt}$ (*Figure 2C*), would be proportional to the calcium current. Higher ζ may reflect a larger depolarization of the neuronal membrane potential. In *Figure 2B-C*, 76% trials (91/120) in the type-I (RF) transition show a positive ramping rate, whereas the proportion rose to 95% (109/115, $p < 0.0001$, χ^2 test) in

the type-II (RT) transition. Among trials longer than 1.5 seconds, they all showed positive ζ , which during the type-II transition was significantly higher than that during the type-I transition (**Figure 2C** and **Figure 2—figure supplement 1C**). These results suggest that the more active AIB are, the more likely a worm would terminate its reversal with a turn.

Optogenetic activation of AIB (*Pnpr-9::ChR2* or *Pnpr-9::Chrimson*) alone reliably triggered reversals followed by omega turns (**Figure 2D**, **Figure 2—figure supplement 1D** and **Video 2**), whereas strong optogenetic inhibition of AIB (*Pmec-4::ChR2*; *Pnpr-9::Arch*; *lite-1*) during ALM/AVM induced escape responses almost completely abolished omega turns (**Figure 2D**). We also generated transgenic animals in which AIB are persistently hyperpolarized by an expression of exogenous potassium channels (*Pnpr-9::TWK-18(gf)*). Interestingly, the no-response fraction increased to ~20% (70/332, $p < 0.0001$, χ^2 test) upon stimulating ALM/AVM in these animals and a significantly larger portion of responses were pauses (35/332, $p < 0.0001$, χ^2 test, **Figure 2E**). We did not observe a significant change in the type-II transition rate r_2 (Kolmogorov-Smirnov test, $p = 0.6$, **Figure 2F**), which might be due to a weaker AIB inhibition in these animals. Furthermore, optogenetic ablation of AIB alone (*Pnpr-9::PH-miniSOG*, **Figure 2—figure supplement 1H**) (Qi, Garren, Shu, Tsien, & Jin, 2012; S. Xu & Chisholm, 2016) significantly suppressed the type-II transition rate (Kolmogorov-Smirnov test, $p < 1e-20$, **Figure 2—figure supplement 1I**). RIM (**Figure 2A**) also promoted reversal (**Figure 2—figure supplement 1B** and **E-G**), but were less important in modulating the type-II transition (**Figure 2—figure supplement 1D-G**). Together, our data strongly suggest that AIB play an important role in promoting reversal and turning behaviors.

Feedforward coupling between the backward module and the turning module drives the omega turn

How do AIB drive turning behaviors? Whole brain imaging in immobilized animals implicated that AIB and their electrically-coupled partners RIV (*Figure 2A and Figure 3—figure supplement 2*) exhibited sequentially activated patterns (Kato et al., 2015). We compared RIV activity patterns (*Plim-4::GCaMP6*) underlying different motor sequences during spontaneous behaviors. During the type-II (RT) transition, RIV calcium signal rose rapidly immediately before a turn began, whereas it remained largely quiescent during the type-I (RF) transition (*Figure 3A and Figure 3—figure supplement 1A*). The calcium signal decayed towards baseline before the animal finished the turn and resumed forward movement (*Figure 3—figure supplement 1B*).

To directly probe the functional connectivity between AIB and RIV, we performed simultaneous optogenetic stimulation of AIB (*Pnpr-9::Chrimson*) and calcium imaging of RIV (*Plim-4::GCaMP6::wCherry*, *Figure 3B*). In immobilized wild-type animals, upon stimulating AIB at $t = 0$, RIV calcium signal rapidly rose (*Figure 3C* dark blue and *Figure 3—figure supplement 1C*). Several innexin, including INX-1, UNC-7 and UNC-9, have been reported to be expressed in AIB and RIV (Altun, Chen, Wang, & Hall, 2009; Bhattacharya, Aghayeva, Berghoff, & Hobert, 2019). Some of these innexins were shown to form homotypic and/or heterotypic gap junctions (Kawano et al., 2011; P. Liu et al., 2013; Todd A Starich, Xu, Skerrett, Nicholson, & Shaw, 2009; T. Xu et al., 2018). To determine whether electrical synapses contribute to the observed functional coupling between AIB and RIV, we examined the effect of AIB stimulation in *inx-1unc-9unc-7* triple innexin mutants. RIV remained quiescent upon AIB stimulation (*Figure 3C* red and *Figure 3—figure supplement 1D*), indicating that gap junction coupling underlies AIB stimulation-mediated RIV calcium activity.

UNC-7 and UNC-9 are broadly expressed in the motor circuit, and *unc-7* or *unc-9* mutants exhibit uncoordinated movements that prohibit them from completing a motor sequence (Barnes & Hekimi, 1997; Brenner, 1974; Kawano et al., 2011; T. A. Starich, Herman, & Shaw, 1993; T. Xu et al., 2018). *inx-1* single mutants exhibit superficially normal forward and backward movements, allowing us to examine the behavioral requirement of INX-1. The presence of multiple innexins in many *C. elegans* neurons implicates that they may function redundantly at electrical synapses. Consistent with this notion, we find that optogenetic activation of AIB was capable, but with less likelihood, to trigger a turn in *inx-1* mutants (**Figure 3D**). Rescuing *inx-1* in AIB was sufficient to restore the turning probability (**Figure 3D**). Because *inx-1* mutants were still capable of generating omega turns, we propose that either multiple innexins between AIB and RIV, or parallel circuit pathways are at play.

When we performed dual optogenetic activation and calcium imaging in wild-type animals that were allowed to move, RIV calcium activity increase was also observed. But we observed a delay in RIV calcium signal, with its increase arriving at variable times (**Figure 3E** and **Figure 3—figure supplement 1F**) instead of an immediately rise after stimulation onset. In many trials, the rise of RIV calcium activity coincided with the initiation of an omega turn (**Figure 3—figure supplement 1F**), an event that was used to realign all trials at $t = 0$ (**Figure 3E** and **Figure 3—figure supplement 1F**).

Delayed activation of RIV in a moving animal may result from a convergence of excitatory- and inhibitory- inputs onto the turning module (**Figure 2A**). When neural activity in behaving animals was aligned to the onset of optogenetic stimulation, a transient quiescence or decrease of RIV calcium activity indeed appeared after $t = 0$ (**Figure 3F** and **Figure 3—figure supplement 1F**). We hypothesized that a rapid increase of calcium activity in **Figure 3C** (dark blue) could

result from a stronger depolarization of RIV neurons in immobilized animals. Consistently, when the calcium imaging experiment in immobilized animals was combined with a weak and persistent optogenetic inhibition of RIV (*Plim-4::Arch*), we also observed a delayed and rectified excitation in RIV (**Figure 3C** light blue and **Figure 3—figure supplement 1E**).

Taken together, our data suggest that the feedforward excitation between the backward module and the turning module takes the form of electrical synapses, likely between AIB and RIV. We considered an effective functional coupling through polysynaptic excitation highly unlikely. First, AIB triggered ventral-biased turning behaviors did not require glutamatergic synaptic transmission (**Figure 4A**), thus excluding polysynaptic pathways via chemical synapses from AIB. Second, two possible polysynaptic excitation pathways from AIB via electrical coupling revealed by the *C. elegans* connectome (White et al., 1986) involve interneurons RIM or RIS (**Figure 3—figure supplement 2**). Our optogenetic activation of AIB while inhibiting RIM did not modify the turning probability, whereas activating RIM while inhibiting AIB significantly reduced the turning probability (**Figure 2—figure supplement 1F-G**). Activation of RIS would drive an animal to a pause state and abolish motor actions (Costa et al., 2019). Both results argue against RIM and RIS being directly involved in driving turning behaviors.

Inhibitory glutamatergic synaptic transmission modulates the type-II transition

We next investigated behavioral flexibility in the timing of an action. Given the feedforward coupling between the backward module and the turning module, we asked why omega turns did not immediately follow the optogenetic activation of AIB. We hypothesized that a balance of feedforward excitation and an unknown inhibition provides a potential mechanism to shape the

statistics of the type-II (RT) transition. Besides gap junctions, AIB make chemical synapses with neurons in other modules (**Figure 2A** and **Figure 4—figure supplement 1A**), which may facilitate this inhibition. AIB are glutamatergic (Serrano-Saiz et al., 2013). In the glutamate vesicular transport deficient mutant *eat-4*, optogenetic activation of AIB robustly induced an omega turn that was preceded by a much shorter reversal (**Figure 4A** left and **Figure 4—figure supplement 1B**). Restoring *eat-4* expression specifically in AIB significantly prolonged the reversal length before the onset of an omega turn (**Figure 4A** left, **Figure 4—figure supplement 1B** and **Video 4**). Likewise, stimulating AIB while blocking chemical synaptic transmission from AIB (*Pnpr-9::TeTx*) triggered an omega turn preceded by a shorter reversal (**Figure 4A** left and **Video 4**). Consistently, r_2 rose more rapidly when glutamatergic inputs from AIB were disrupted (**Figure 4A** right).

C. elegans nervous system possesses a family of inhibitory glutamate-gated chloride (GluCl) channels (Dent, Davis, & Avery, 1997). Upon optogenetic stimulation AIB, the triple GluCl mutant *avr-14(ad1035);avr-15(vu227)glc-1(pk54)* exhibited a behavioral phenotype resembling that of the *eat-4* mutant (**Figure 4B** and **Figure 4—figure supplement 1B**). In some trials (19/112, $p < 0.0001$, Fisher's exact test), AIB stimulation immediately triggered omega turns without delay (**Video 4**). This suggests that postsynaptic GluCl receptors work synergistically in modulating the onset timing of a turn. Using GFP reporter lines, we found *avr-14*, *glc-1* and *avr-15* expressed in many neurons. By focusing on overlaps with neurons known to encode motor states (**Figure 2A**), we found that *Pavr-14* and *Pglc-1* reporters exhibited expression in the AIY interneurons, while the *Pavr-15* reporter exhibited expression in RIB interneurons (**Figure 4C**).

Unlike AIY, RIB receive more and invariant synaptic inputs from AIB (White et al., 1986; Witvliet et al., 2020) (**Figure 2A**), and hence the prominent and invariant postsynaptic partners of AIB. Consistent with a glutamate mediated feedforward inhibition, RIB calcium activity (*Psto-3::GCaMP6*) significantly reduced upon optogenetic activation of AIB in immobilized animals, which was not observed in the glutamate vesicular transport deficient mutant *eat-4* animals (**Figure 4D** and **Figure 4—figure supplement 1C**). Moreover, restoring either *avr-15* expression in RIB or the *avr-14* (or *glc-1*) expression in AIY promoted a longer reversal before the onset of an omega turn (**Figure 4B** and **Video 4**) upon AIB activation.

To investigate the functional connectivity between AIB and RIB, we imaged glutamate signaling (Marvin et al., 2013) at RIB (*Psto-3::iGluSnFR*) upon persistent optogenetic stimulation of AIB (*Pnpr-9::Chrimson*; see Materials and Methods). After the onset of stimulation, a rapid rise (**Figure 4E** inset plot, $\sim 10\% \Delta F/F_0$) of iGluSnFR signal on RIB's neurites (**Figure 4E** and **Figure 4—figure supplement 2A** up) followed by a slow decay. The fluorescence signal change was well fit by

$$\frac{\Delta F(t)}{F_0} = B \left(e^{-\frac{t}{\tau_1}} - e^{-\frac{t}{\tau_2}} \right), \quad Eq. (1)$$

where $\tau_1 = 0.9 \text{ s}$, and $\tau_2 = 100 \text{ ms}$. In animals without feeding all-trans retinal (a co-factor required for AIB optogenetic stimulation in this experiment), we observed random and smaller amplitude ($\sim 5\% \Delta F/F_0$) fluctuations of iGluSnFR signals (**Figure 4E**). Such dynamics was not observed in the glutamate vesicular transport deficient mutant *eat-4* animals (**Figure 4E** and **Figure 4—figure supplement 2A** bottom).

276

277 **Local interneurons RIB promote both turning and forward behaviors**

278 Local interneurons RIB, together with the ventral cord projection premotor interneurons AVB,
279 have been previously reported to encode forward movement state (Gray et al., 2005; Kato et al.,
280 2015; Li et al., 2014). Moreover, RIB form gap junctions with SMDV (**Figure 2A**), motor neurons
281 that have also been implicated in ventral biased omega turns (Gray et al., 2005; White et al., 1986).
282 RIB calcium activity declined during reversals, and rose during the type-I (RF) and type-II (RT)
283 transitions (**Figure 5A** and **Figure 5—figure supplement 1A**), which is characteristic of neurons
284 in both forward and turning modules (**Figure 2A**).

285 Optogenetic manipulation of RIB in freely behaving animals further revealed their functions
286 during motor control. Activating RIB (*Psto-3::Chrimson*) during reversals triggered a transition to
287 either an omega turn or forward movement (**Figure 5B** left). Strong optogenetic activation (635
288 nm, 3.75 mW/mm²) of RIB during forward movement reliably triggered omega turns (**Figure 5B**
289 right and **Video 5**). On the other hand, inhibiting RIB (*Psto-3::Arch*) during forward movement
290 led to a pause (**Figure 5B** right and **Video 5**).

291 When RIB interneurons were directly inhibited to mimic an inhibitory synaptic input, either
292 optogenetically or by an expression of histamine-gated chloride channels (Pokala, Liu, Gordus, &
293 Bargmann, 2014), the type-II (RT) transition rate r_2 plateaued at a significantly reduced value
294 (**Figure 5C** and **Figure 5—figure supplement 1B**). Consistently, an escape response comprised
295 of a much longer reversal before an omega turn was initiated (**Figure 5C**, **Figure 5—figure**
296 **supplement 1B** and **Video 6**), in agreement with the GluCl rescue results (**Figure 4B** left). The
297 type-I transitions were also largely suppressed (**Figure 5C**), as RIB potentiate forward movements.

Optogenetic ablation (*Psto-3::miniSOG*) or blocking chemical synaptic transmission (*Psto-3::TeTx*) from RIB also led to prolonged reversals during ALM/AVM-triggered escape responses (**Figure 5F**).

We asked how RIB may mediate neural activity in the turning module. Upon optogenetic stimulation of AIB (**Figure 5D-E**), the rise of RIV calcium activity in RIB ablated animals showed the same rectified activation when all trials were aligned to the beginning of a turn (**Figure 5E**). However, RIV activity was preceded by a longer quiescent state when trials were aligned to the stimulus onset (**Figure 5D** and **Figure 5—figure supplement 1C**). Thus, RIB modulate motor state transitions in part through indirect modulation of the timing of RIV activation (**Figure 2A**).

Inhibitory feedback contributes to reversal termination

The beginning of a turn marks the end of a reversal. We next asked whether the type-II (RT) transition can be accounted for by self-termination of neural activity in the backward module (**Figure 2A**), analogous to a feedforward synaptic chain model, or, whether activation of the turning module provides a feedback to terminate the activity in the backward module.

In a feedforward synaptic chain model, perturbing neural activity in the downstream neurons would not affect the dynamics of upstream neurons. To test this model, we generated transgenic animals that express Archaeorhodopsin in RIV/SAA/SMB neurons (*Plim-4::Arch*; **Figure 6A**). RIV/SAAD/SMB all exhibited elevated calcium activity during omega turns (**Figure 5—figure supplement 1D**). However, optogenetic inhibition of RIV/SAA/SMB or RIV alone by spatially

patterned illumination during escape responses promoted significantly longer reversals (**Figure 6B** and **Video 6**).

Observations from optogenetic ablation of RIV/SAA/SMB (*Plim-4::miniSOG*) also argue against a pure feedforward synaptic chain model. The type-II transition was abolished since animals could no longer generate a complete omega turn (**Figure 6C** upper panel), while the ability for animals to directly transition from backward to forward movements remained unaffected and the type-I (RF) transition rate r_1 remained similar (**Figure 6C** upper panel) to wild-type animals. Notably, the reversal duration became much longer and approached 30 seconds in some trials, which had not been observed in wild-type animals (**Figure 1C**, **6C** upper panel and **Video 3**). These results indicate that during normal type-II transitions, persistent neural activity in the upstream backward module could be abolished through inhibitory feedback from the downstream activity in the turning module.

Both the type-I (RF) transition rate (**Figure 6C** upper panel) and the mirror transition rate (FR) from a forward movement to a spontaneous reversal in wild-type animals (**Figure 6C** bottom panel) are consistent with the homogeneous Poisson process at long timescale, leading to exponential survival functions (**Figure 6C** insets) — fraction of backward or forward movements survived to t (Berg, 1993; Stephens, Bueno de Mesquita, Ryu, & Bialek, 2011). We did not observe an exponential survival function of reversals in wild-type animals. In the absence of the turning module, the statistics of forward and backward movements (**Figure 6C**) became consistent with a simple dynamic model, where a system stochastically transitions between two attractor states with constant rates.

Together, our data suggest that the feedforward inhibition (**Figure 4**) and feedback inhibition (**Figure 6**) between the backward module and the turning module implement a winner-take-all computation for action selection. The motor module with the highest level of activity stays active by suppressing the activities of other modules.

A biophysical model of the type-II transition

With both structural and functional evidence, we now propose a mathematical model for the type-II (RT) transition. The turning module, represented by RIV inter/motor neurons, receives opposing excitatory and inhibitory inputs during backward movements (**Figure 7A**). The rapid increase of RIV activity coincides with the beginning of an omega turn (**Figure 3A, 3E**). To capture the essential process, we assumed that the membrane potential of RIV x fluctuates around a balanced state x_0 during a reversal (**Figure 7B**), and its neural dynamics is governed by the Langevin equation:

$$\frac{dx}{dt} = -k(x - x_0) + \eta, \quad x < x_{th} \quad Eq. (2)$$

where k depends on, among others, the gap junction and inhibitory synaptic conductances (see Appendix); and η could be regarded as fluctuations in synaptic currents (Lindsay, Thiele, & Lockery, 2011; Narayan, Laurent, & Sternberg, 2011) and other sources of noises that are not explicitly considered in the model. For simplicity, η is treated as uncorrelated Gaussian white noise: $\langle \eta(t)\eta(t') \rangle = 2\sigma^2\delta(t - t')$. Once the membrane potential crosses the threshold x_{th} , RIV become rapidly depolarized due to a nonlinear rectified activation (**Figure 7B**), immediately terminating

the reversal via feedback inhibition and starting a turn by activating ventral muscles (**Figure 7A** and **7D**).

The next step is to calculate the type-II transition rate r_2 : the probability that x crosses x_{th} per unit time. It is currently impossible to measure k , but we can proceed by making a non-trivial prediction. Based on electrophysiological recordings of *C. elegans* interneurons (Lindsay et al., 2011; Roberts et al., 2016), the membrane time constant of a neuron (~ 10 milliseconds) is much smaller than the behavioral timescale (\sim seconds). As a result, the membrane potential of a model neuron rapidly approaches the stationary state x_0 . By solving this problem analytically using one-dimensional Fokker-Planck equation near the system equilibrium (see Appendix), we find

$$r_2 \approx \frac{k}{\pi} \operatorname{erfi}^{-1} \left[\sqrt{\frac{k}{2\sigma^2}} (x_{th} - x_0) \right] \quad \text{Eq. (3)}$$

Here $\operatorname{erfi}(x) = \frac{2}{\sqrt{\pi}} \int_0^x e^{z^2} dz$ is the imaginary error function.

Eq. (3), however, would lead to a constant rate on the behavioral timescale, like that during the type-I (RF) transition, as expected and confirmed by our computer simulation (**Figure 7C**). To explain the experimental observation of the rising phase of r_2 (**Figure 1C-D**), we incorporated a plasticity mechanism analogous to short-term synaptic depression (STD): the feedforward inhibition from the backward module to the turning module becomes weaker as the reversal lasts longer (**Figure 7D**). Consequently, the membrane potential moves towards the excitation threshold x_{th} to potentiate transition, allowing the analytical expression for r_2 , Eq. (3), to become time-dependent. Our hypothesis is consistent with the decay of the glutamate sensor signal on RIB neurites upon AIB stimulation (**Figure 4E**), an observation that may be explained by a depletion of available vesicles for release at the presynaptic site. Note that calcium activity in AIB cell body,

like that during a reversal (**Figure 2B**), kept increasing during persistent optogenetic stimulation (**Figure 4—figure supplement 2B**), arguing against the possibility that an opsin-mediated membrane depolarization in the presynaptic neuron undergoes depression upon continuous light activation.

By incorporating the exponential decay of inhibitory synaptic strength (Eq. 1), we found that the functional form of the transition rate (see Appendix) can be approximated by

$$r_2(t) \approx k_1 \operatorname{erfi}^{-1}(k_2 + k_3 e^{-t/\tau_g}), \quad \text{Eq. (4)}$$

where $\tau_g = 0.9 \text{ s}$ is the decay constant of the glutamate signal (**Figure 4E**). The experimentally measured type-II transition rate is well fit by Eq. (4), whereas the standard sigmoid function, $\frac{1}{k_1 + k_2 e^{-t/\tau}}$, with the same number of free parameters provides a worse fit at the short timescale (**Figure 7E**).

Discussion

Complex motor behaviors arise from continual selection and transition among a number of motor primitives. Classic synaptic chain models, in which stereotyped motor sequences arise from feedforward excitation between different groups of neurons, are thought to underlie several motor behaviors such as Zebra Finch singing (Long et al., 2010). A feedforward synaptic chain may underlie the replay of spatiotemporal activity patterns in hippocampus during sleep (Louie & Wilson, 2001; Skaggs & McNaughton, 1996), and generate temporally precise firing patterns that correspond to different actions in the motor cortex of behaving monkeys (Shmueli et al., 2006). Alternatively, when several mutually inhibited modules are co-activated by sensory inputs, motor sequences could also emerge by a winner-take-all strategy, a proposed mechanism for the grooming behavior in *Drosophila* (Seeds et al., 2014). In mice, mutually inhibitory neurons in the central amygdala have been shown to regulate dimorphic defensive behaviors — flight or freezing — triggered by looming visual stimuli (Fadok et al., 2017). Here, we find the two schemes are likely integrated by the *C. elegans* nervous system to generate robust and flexible motor sequences (**Figure 7D**).

In *C. elegans*, feedforward excitation between the backward module and the turning module (**Figure 7A**) can reliably trigger an omega turn followed by forward movement through strong and persistent activation of local interneurons AIB (**Figure 2D** and **Figure 2—figure supplement 1D**). In other words, the action in a motor sequence can be selected through feedforward excitation, triggered by either external sensory stimulus or fluctuations of internal circuit dynamics. The timing of an action can be tuned by augmenting the feedforward excitation with glutamatergic feedforward inhibition between AIB and RIB (**Figure 7A**), likely through modulating the strength

of inhibitory inputs through short term synaptic plasticity. Previously, a tyraminergetic feedforward inhibition (Alkema, Hunter-Ensor, Ringstad, & Horvitz, 2005; Pirri et al., 2009) from the RIM interneurons in the backward module to the SMD motor neurons in the turning module was shown to suppress head movement during reversals. We propose that these functional motifs — feedforward excitation and inhibition — are combined with a nonlinear activation of turning neurons (**Figure 7D**) to produce flexible type-II (RT) transitions.

A simple synaptic chain model predicts that abolishing neural activity in a downstream module would not directly affect upstream neural output. However, when RIV/SAA/SMB in the turning module were ablated or inhibited (**Figure 6B-C**), we observed prolonged reversals during escape responses. Hence, the turning module may provide feedback inhibition onto the backward module, contributing to the reversal termination during type-II transitions. The cellular and molecular mechanisms for inhibitory feedback remain to be identified. One possible implementation is cholinergic synaptic outputs from SAAD onto RIM and AVA interneurons in the backward module; another possibility is synaptic outputs from RIB onto AVA/AVE (**Figure 7A**). Together, the feedforward coupling between the backward module and the turning module facilitates a defined sequential activity pattern, whereas the winner-take-all operation through mutual inhibition between the two modules avoids an action conflict.

Sensorimotor transformation depends on the initial condition of the network state (Remington, Egger, et al., 2018; Remington, Narain, Hosseini, & Jazayeri, 2018). We show that when the backward motor state is suppressed via the hyperpolarization of interneurons AIB, an identical mechanosensory stimulus is less likely to elicit an escape response (**Figure 2E**). A recent study also demonstrated that mechanosensory stimuli were unlikely to drive other motor programs when

C. elegans was executing a turn (M. Liu et al., 2018). We propose that the inhibition from the turning module to the backward module (**Figure 7D**) may account for this observation.

We view omega turn, a motor state encoded by transient activity in RIV, as a special manifold connecting two attractors represented by persistent activity in the forward or backward module (**Figure 7D**). In our simplified model, neurons within a module were treated as a homogeneous population. Nevertheless, interneurons with heterogeneous functional properties have been found. For example, laser ablation of AIB and RIM in the backward module (**Figure 2A**) differentially affect the probability of spontaneous reversals (Gray et al., 2005). While RIM showed increased calcium activity during reversals (**Figure 2—figure supplement 1B**) and promoted reversal duration upon optogenetic activation (**Figure 2—figure supplement 1E-G**), they were less important in modulating the type-II transition than AIB did (**Figure 2—figure supplement 1D-G**). The impact of functional heterogeneity on the attractor dynamics and motor state transitions remains to be understood.

Our biophysical model suggests that noises in a neural circuit (Eq. 2) contributes to behavior variability. We speculate that stochasticity in neural dynamics and behaviors may allow animals to efficiently explore the action space (Dhawale et al., 2017; Tumer & Brainard, 2007); learning, by which functional connectivity between motor modules is modified through synaptic plasticity, may optimize action selection and timing (Sutton & Barto, 2017). We found that in *C. elegans*, the functional connectivity between motor modules comprises of feedforward excitation and mutual inhibition. Conserved network motifs may be distributed among mammalian forebrain and midbrain circuits (Fadok et al., 2017; Klaus, Alves da Silva, & Costa, 2019). Other animals could use similar algorithms to organize neuronal activities into sequential states to drive motor primitives, by which stereotyped and flexible behaviors emerge.

Acknowledgments

We thank Louis Tao for discussions, Pinjie Li for analyzing the reorientation angles during the type-I and type-II transitions. This work was funded by National Science Foundation of China Grants NSFC-31471051 and NSFC-91632102, the Strategic Priority Research Program of the Chinese Academy of Sciences (Pilot study, grant XDPB10, Grant No. XDB39000000), the Guangdong Province with Grant No. 2018B030338001, the CAS Hundreds Talent Plan, and the Fundamental Research Funds for the Central Universities (QW), and the Canadian Institute of Health Research Foundation Scheme 154274 (MZ). Mei Zhen thanks her lab members Yangning Lu, Maria Lim, and Jyothsna Chitturi for sharing their unpublished optogenetic methods, observations, and reagents used in this study.

Declaration of Interests

The authors declare no competing interests.

472 **Materials and Methods**

473 **Key resources table**

Key Resources Table				
Reagent type (species) or resource	Designation	Source or reference	Identifiers	Additional information
Strain, strain background (<i>C. elegans</i>)	<i>C. elegans</i> strains used and generated in this study	<i>Caenorhabditis</i> Genetics Center (CGC) and this paper		<i>Supplementary File 1</i>
Recombinant DNA reagent	Plasmids generated in this study	This paper		<i>Supplementary File 2</i>
Recombinant DNA reagent	Primers for genes (or promoters) used in this study	This paper		<i>Supplementary File 3</i>
Software, algorithm	MATLAB	Mathworks	RRID:SCR_001622	https://www.mathworks.com
Software, algorithm	CoLBeRT system	Samuel Lab		http://colbert.physics.harvard.edu/
Software, algorithm	ImageJ	Media Cybernetics	RRID:SCR_003070	https://imagej.net/
Software, algorithm	LabVIEW	National Instruments	RRID:SCR_014325	http://www.ni.com

475 ***C. elegans* Strains**

476 *C. elegans* strains including wild-type (N2), mutants, and transgenic worms were grown and
 477 cultivated according to standard procedures (Brenner, 1974). All strains used in this paper can be

found in the *Supplementary File 1*. Transgenic worms for optogenetic experiments were cultivated in dark on NGM plates with OP50 bacteria and 0.4 mM all-trans retinal (ATR) for over 5 hours. We used young adult hermaphrodites to perform optogenetic and calcium imaging experiments, and L4 hermaphrodites to obtain expression patterns.

Molecular biology

Standard molecular biology methods were used. Details of plasmids, the promoters and rescue genomic DNA (or cDNA) sequences can be found in *Supplementary File 2-3*.

Optogenetics

Worms were first washed in M9 buffer (or transferred onto an unseeded NGM plate for 1-3 minutes), then transferred onto a fresh agar plate [$\sim 0.8\%$ (w/v) agar in M9 buffer, without food], mounted on a motorized stage. Worms were left to freely explore the new environment for 3-5 minutes before testing, and were automatically tracked and retained within the field of view of a 10 \times objective (Nikon Plan Apo, NA = 0.45) mounted on an inverted microscope (Nikon Ti-U, Japan) via dark field infrared illumination. Worm behaviors were recorded by a CMOS camera (Basler, aca2000-340kmNIR, Germany). MATLAB custom software (MathWorks, Inc. Natick, MA, USA) was used for post-processing behavioral data and extracting moving directions and the kinematics of omega turns.

For freely roaming worms without optogenetic stimulation, we only recorded them for 5-8 minutes.

For worms with optogenetic stimulation, lasers and a digital micromirror device (DLI4130 0.7 XGA, Digital Light Innovations, TX, USA) were used to generate a defined spatiotemporal

illumination pattern (Leifer et al., 2011) at a specific wavelength (473 nm, 561 nm or 635 nm), and to manipulate the activities of neurons expressing light-activated channels (ChR2, Arch or Chrimson) (Husson et al., 2012; Nagel et al., 2005). To eliminate the effect of adaptation, single worm was stimulated 5-8 times with at least a 50 -second inter-stimulus interval. For example:

(1) To trigger escape responses, worms received 1.5 s blue light (short enough and over 80% trials showed responses in pilot experiments) to activate mechanosensory neurons ALM/AVM. All worms in the dataset had at least 20% probability to perform either type-I or type-II transitions. In other cases, 7 s (or 12 s) optogenetic illumination were used to ensure persistent activation/inhibition of local interneurons.

(2) In some experiments, worms received sequential optogenetic stimulations with different colors and varying durations controlled by diaphragm shutters (GCI 7102M, Daheng Optics, China). For example, the 1.5 s blue light optogenetic stimulation (to trigger escape response) was followed by green light with a duration of 3-12 s to inhibit other interneurons in the motor control circuit.

(3) We also performed selective optogenetic manipulation of interneurons when their cell body positions were sufficiently apart, given that the lateral resolution of our CoLBeRT system is up to $\sim 5 \mu\text{m}$. For example, RIV and SAAD neurons are separated by at least $20 \mu\text{m}$ along the dorsal-ventral axis (**Figure 6A**). In order to inhibit SAAD or RIV independently (*Plim-4::Arch::GFP*), we generated a spatial pattern to selectively illuminate the dorsal or ventral side (**Figure 6B** right). At the same time, we monitored GFP emission signals from these neurons excited by the laser (473 nm) to ensure we targeted the correct region (**Figure 6B**).

Calcium imaging

Calcium imaging was conducted on worms expressing a GCaMP6::wCherry (or mCardinal) fusion protein. Calcium activity was measured as a ratiometric change. For example, neural activity of AIB was measured as a fluorescence ratio of GFP to RFP ($\Delta R(t)/R_0$) (GCaMP6/wCherry), where R_0 is the baseline ratio. In some cases, we define a new normalized ratiometric measure, $\Delta \tilde{R}(t) = [\Delta R(t) - \Delta R(t=0)]/R_0$.

When cell-specific promoters are available, including AIB and RIB, we performed calcium imaging using wide-field fluorescence microscopy. Unrestrained behaving worms were placed on fresh agarose plates [2% (w/v) agarose in M9 buffer], tracked by a motorized stage using the CoLBeRT system with infrared light illumination (Leifer et al., 2011). Blue and green lights were employed to excite GCaMP6 and wCherry (or mCardinal) proteins. Green and red emission signals were captured by a 10× objective (Nikon Plan Apo, WD = 4 mm; NA = 0.45, Japan) at 50 fps with an exposure time of 20 ms, separated by a dichroic mirror, relayed by an optical splitter (OptoSplit II, Cairn-Research, UK), and projected onto one-half of a sCMOS sensor (Andor Zyla 4.2, UK) simultaneously. Green and red channels were aligned and processed by custom-written MATLAB scripts (T. Xu et al., 2018). Single worm was recorded for 3-10 min.

To image RIV neurons, which lack cell-specific promoters, we picked transgenic worms (*Plim-4::GCaMP6::wCherry*) with stronger fluorescence expression on RIV, and increased the exposure time (up to 50 ms) to obtain high signal-to-noise ratio images.

Multi-neuron calcium imaging in a freely behaving worm

To image calcium activity of multiple neurons in a freely behaving worm (e.g., **Figure 2-figure supplement 1B**), we combined a spinning disk confocal inverted microscope (Nikon Ti-U & Yokogawa CSU-W1, Japan) for calcium imaging with a customized upright light path for worm

tracking and behavior recording. A worm was placed on an agarose pad [$\sim 2\%$ (w/v)] mounted on a motorized stage. We used a 40 \times air objective (Nikon Plan Apo, WD 0.25-0.17 mm; NA = 0.95, Japan) or a 60 \times water immersion objective (Nikon Plan Apo, WD 0.22 mm; NA = 1.20, Japan). The wavelengths of confocal excitation lasers were 488 nm and 561 nm; the emission lights were split (Andor Optosplit II, UK) in front of a sCMOS camera (Andor Zyla 4.2, UK). At the same time, we utilized a customized light path that was aligned to the same z axis to track the worm and to record behavioral data. In the upright path, a low magnification 10 \times objective (Nikon Plan Fluor, WD 16 mm; NA = 0.30, Japan) was used to gather fluorescent light excited by confocal lasers, and the fluorescent signal was processed to identify worm positions. A real time feedback signal was sent to a motorized stage to keep the worm head within the center of field of view. Meanwhile, we illuminated the worm by an infrared ring surrounding the high magnification objective to record worm behavior through the upright light path.

Simultaneous optogenetic manipulation and calcium imaging

To combine calcium imaging and optogenetic manipulation (e.g., **Figure 3B**), a 635 nm laser was added to activate Chrimson. Because blue light can also activate Chrimson, excitation light for GCaMP6 imaging and red light for optogenetic stimulation were synchronized using a TTL signal (LabJack Corp., U3-HV) controlled by LabVIEW (National Instruments Corp., USA). For example, to verify the connectivity between AIB and RIV, we activated AIB using red laser (635 nm) and recorded the calcium signal in RIV using blue LED excitation (M470L3-C1; Thorlabs, USA) for 7 seconds simultaneously. Both restrained and freely moving worms were tested. Restrained worms were placed on 10% (w/v) agarose plates with coverslips, whereas freely moving ones were placed on 2% (w/v) fresh agarose plates. Single worm was stimulated 5-8 times with at least a 50 s inter-trial interval.

Thermally-induced escape responses

In addition to optogenetic stimulation of mechanosensory neurons, we also used a thermal stimulus to trigger escape responses. We illuminated the head of a worm with a focused infrared laser light (1480 nm; spot diameter ~120 μm , $\Delta T \sim 2^\circ\text{C}$) for 0.75 s (short enough and over 80% trials showed responses in pilot experiments), and animals responded with reversals or omega turns to avoid the stimulus (Mohammadi et al., 2013). The transition rates were qualitatively similar to ALM/AVM-induced escape responses (**Figure 1C-D**). Identical experimental protocols were used when thermally-induced escape responses were followed by optogenetic manipulation or calcium imaging of interneurons.

Glutamate imaging

Glutamate imaging was conducted on worms expressing iGluSnFR (Marvin et al., 2013) on RIB and Chrimson on AIB (**Figure 4E** and **Figure 4—figure supplement 2A**). All worms were restrained on fresh 10% (w/v) agarose plates with coverslips. We used 60 \times water immersion objective. Both processes and cell body of RIB were imaged on the same focal plane. Imaging acquisition rate is 150 fps. Like calcium imaging, blue excitation light (weak enough to reduce the bleaching effect; M470L3-C1; Thorlabs) for glutamate imaging and red light (635 nm, 6.11 mW/mm²) for optogenetic stimulation were synchronized with a TTL signal. Glutamate signaling resulted in a change of the green fluorescence signal on the membrane of RIB interneurons. Stimulation and imaging sustained for more than 8 seconds. Single worm was stimulated 2-3 times with at least a 50 s inter-stimulus interval.

Optogenetic ablation

We used miniSOG (mini Singlet Oxygen Generator) to ablate specific neurons in *C. elegans*. Upon blue light stimulation, a mitochondria-targeted miniSOG (TOMM20-miniSOG) (Qi et al., 2012) and a membrane-targeted miniSOG (PH-miniSOG) (S. Xu & Chisholm, 2016) were employed to induce cell death in cell-autonomous manner. L2/early L3 worms were transferred onto an unseeded NGM plate, restricted by a small ring of filter paper soaked with 100 μ M CuCl₂. Worms were illuminated for 40-60 min (TOMM20-miniSOG) or 2 min (PH-miniSOG) with blue LED (M470L3-C5; Thorlabs) at the intensity of 0.46 mW/mm². After illumination, worms were transplanted back to OP50-seeded NGM plates, allowed to recover for 1-2 days before behavior testing.

Behavioral assays and analysis

Recorded movies, in which worm body centerlines were extracted in real time, were further processed semi-automatically in MATLAB to identify locomotor states (forward locomotion, backward locomotion, pause and turn) and other statistical parameters. We also set up a Graphic User Interface (GUI) that allows human interference and proofreading.

Reversal duration was defined as the time from reversal start to reversal end. If one stimulus triggered several reversals, we always scored the first one. Omega turns were identified by either the head touching the body (or tail) or $\theta > 135^\circ$ within a single head swing (*Figure 1—figure supplement 1A*). The end of a turn was identified when a worm opened its coiled posture and began to move forward.

Transition rate calculation

Transition rates are calculated by the following equation

$$\begin{aligned}
r_i(t_0) &\approx \frac{\int_{t_0 - \frac{\Delta t}{2}}^{t_0 + \frac{\Delta t}{2}} r_i(t) dt}{\Delta t} \approx \frac{\int_{t_0 - \frac{\Delta t}{2}}^{t_0 + \frac{\Delta t}{2}} p_i(t) dt}{\Delta t \left[1 - \int_0^{t_0 - \frac{\Delta t}{2}} (p_1(t) + p_2(t)) dt \right]} \\
&= \frac{N_i \left(t_0 - \frac{\Delta t}{2} \right) - N_i \left(t_0 + \frac{\Delta t}{2} \right)}{\Delta t [N_1 \left(t_0 - \frac{\Delta t}{2} \right) + N_2 \left(t_0 - \frac{\Delta t}{2} \right)]}
\end{aligned}$$

Here $i = 1, 2$, represents type-I or type-II transition. $r_i(t)$ is the transition rate, $p_i(t)$ is the probability density function of the two transitions, $N_i(t)$ is the total number of reversals that survive to t for a given transition type, and Δt denotes the bin width.

Theoretical account of transition rates and model details

Detailed description can be found in Appendix.

Quantification and statistical analysis

Quantification and statistical parameters were indicated in the legends of each figure, including the statistical methods, error bars, n numbers (see *Supplementary File 4* for more details), and p values. We applied Mann–Whitney U test, χ^2 test or Fisher’s exact test among samples, two-way ANOVA to determine the significance of difference between groups for two factors, and Kolmogorov–Smirnov test to compare probability distributions from two samples. All multiple comparisons were adjusted using Bonferroni correction. We considered p values of < 0.05 significant. All analyses were performed using MATLAB.

Data availability

623 Raw data of calcium imaging experiments and all code used for modeling or figure generation are
624 available for download from <https://github.com/Wenlab/Worm-Motor-Sequence-Generation>.
625 Source data files have been provided for main figures.

- 627 Abeles, M. (1991). *Corticonics: Neural Circuits of the Cerebral Cortex*: Cambridge University Press.
- 628 Alkema, M. J., Hunter-Ensor, M., Ringstad, N., & Horvitz, H. R. (2005). Tyramine Functions
629 independently of octopamine in the *Caenorhabditis elegans* nervous system. *Neuron*, 46(2), 247-
630 260. doi:10.1016/j.neuron.2005.02.024
- 631 Allen, C., & Stevens, C. F. (1994). An evaluation of causes for unreliability of synaptic transmission. *Proc*
632 *Natl Acad Sci U S A*, 91(22), 10380-10383. doi:10.1073/pnas.91.22.10380
- 633 Altun, Z. F., Chen, B., Wang, Z. W., & Hall, D. H. (2009). High resolution map of *Caenorhabditis elegans*
634 gap junction proteins. *Dev Dyn*, 238(8), 1936-1950. doi:10.1002/dvdy.22025
- 635 Barnes, T. M., & Hekimi, S. J. J. o. n. (1997). The *Caenorhabditis elegans* avermectin resistance and
636 anesthetic response gene *unc-9* encodes a member of a protein family implicated in electrical
637 coupling of excitable cells. 69(6), 2251-2260.
- 638 Berg, H. C. (1993). *Random Walks in Biology*. Princeton, New Jersey.
- 639 Berman, G. J., Choi, D. M., Bialek, W., & Shaevitz, J. W. (2014). Mapping the stereotyped behaviour of
640 freely moving fruit flies. *J R Soc Interface*, 11(99). doi:10.1098/rsif.2014.0672
- 641 Bhattacharya, A., Aghayeva, U., Berghoff, E. G., & Hobert, O. (2019). Plasticity of the Electrical
642 Connectome of *C. elegans*. *Cell*, 176(5), 1174-1189 e1116. doi:10.1016/j.cell.2018.12.024
- 643 Brenner, S. (1974). The genetics of *Caenorhabditis elegans*. *Genetics*, 77(1), 71-94.
- 644 Burak, Y., & Fiete, I. R. (2012). Fundamental limits on persistent activity in networks of noisy neurons.
645 *Proc Natl Acad Sci U S A*, 109(43), 17645-17650. doi:10.1073/pnas.1117386109
- 646 Chalfie, M., Sulston, J. E., White, J. G., Southgate, E., Thomson, J. N., & Brenner, S. (1985). The neural
647 circuit for touch sensitivity in *Caenorhabditis elegans*. *J Neurosci*, 5(4), 956-964.
- 648 Costa, W. S., Van der Auwera, P., Glock, C., Liewald, J. F., Bach, M., Schüler, C., . . . Bringmann, H. J.
649 N. c. (2019). A GABAergic and peptidergic sleep neuron as a locomotion stop neuron with
650 compartmentalized Ca²⁺ dynamics. *Nature communications*, 10(1), 1-15.
- 651 Dent, J. A., Davis, M. W., & Avery, L. J. T. E. j. (1997). *avr-15* encodes a chloride channel subunit that
652 mediates inhibitory glutamatergic neurotransmission and ivermectin sensitivity in *Caenorhabditis*
653 *elegans*. *The EMBO journal*, 16(19), 5867-5879.
- 654 Dhawale, A. K., Smith, M. A., & Olveczky, B. P. (2017). The Role of Variability in Motor Learning. *Annu*
655 *Rev Neurosci*, 40, 479-498. doi:10.1146/annurev-neuro-072116-031548
- 656 Fadok, J. P., Krabbe, S., Markovic, M., Courtin, J., Xu, C., Massi, L., . . . Luthi, A. (2017). A competitive
657 inhibitory circuit for selection of active and passive fear responses. *Nature*, 542(7639), 96-100.
658 doi:10.1038/nature21047
- 659 Ganguli, S., Bisley, J. W., Roitman, J. D., Shadlen, M. N., Goldberg, M. E., & Miller, K. D. (2008). One-
660 dimensional dynamics of attention and decision making in LIP. *Neuron*, 58(1), 15-25.
661 doi:10.1016/j.neuron.2008.01.038
- 662 Gordus, A., Pokala, N., Levy, S., Flavell, S. W., & Bargmann, C. I. (2015). Feedback from network states
663 generates variability in a probabilistic olfactory circuit. *Cell*, 161(2), 215-227.
664 doi:10.1016/j.cell.2015.02.018
- 665 Gray, J. M., Hill, J. J., & Bargmann, C. I. (2005). A circuit for navigation in *Caenorhabditis elegans*. *Proc*
666 *Natl Acad Sci U S A*, 102(9), 3184-3191. doi:10.1073/pnas.0409009101
- 667 Harvey, C. D., Coen, P., & Tank, D. W. (2012). Choice-specific sequences in parietal cortex during a
668 virtual-navigation decision task. *Nature*, 484(7392), 62-68. doi:10.1038/nature10918
- 669 Husson, S. J., Liewald, J. F., Schultheis, C., Stirman, J. N., Lu, H., & Gottschalk, A. (2012). Microbial
670 light-activatable proton pumps as neuronal inhibitors to functionally dissect neuronal networks in
671 *C. elegans*. *PLoS One*, 7(7), e40937. doi:10.1371/journal.pone.0040937
- 672 Iino, Y., & Yoshida, K. (2009). Parallel use of two behavioral mechanisms for chemotaxis in
673 *Caenorhabditis elegans*. *J Neurosci*, 29(17), 5370-5380. doi:10.1523/JNEUROSCI.3633-08.2009

- Inagaki, H. K., Inagaki, M., Romani, S., & Svoboda, K. (2018). Low-Dimensional and Monotonic Preparatory Activity in Mouse Anterior Lateral Motor Cortex. *J Neurosci*, 38(17), 4163-4185. doi:10.1523/JNEUROSCI.3152-17.2018
- Kato, S., Kaplan, H. S., Schrodell, T., Skora, S., Lindsay, T. H., Yemini, E., . . . Zimmer, M. (2015). Global brain dynamics embed the motor command sequence of *Caenorhabditis elegans*. *Cell*, 163(3), 656-669. doi:10.1016/j.cell.2015.09.034
- Kawano, T., Po, M. D., Gao, S., Leung, G., Ryu, W. S., & Zhen, M. (2011). An imbalancing act: gap junctions reduce the backward motor circuit activity to bias *C. elegans* for forward locomotion. *Neuron*, 72(4), 572-586. doi:10.1016/j.neuron.2011.09.005
- Klaus, A., Alves da Silva, J., & Costa, R. M. (2019). What, If, and When to Move: Basal Ganglia Circuits and Self-Paced Action Initiation. *Annu Rev Neurosci*, 42, 459-483. doi:10.1146/annurev-neuro-072116-031033
- Laurent, P., Soltesz, Z., Nelson, G. M., Chen, C., Arellano-Carbajal, F., Levy, E., & de Bono, M. (2015). Decoding a neural circuit controlling global animal state in *C. elegans*. *Elife*, 4. doi:10.7554/eLife.04241
- Leifer, A. M., Fang-Yen, C., Gershow, M., Alkema, M. J., & Samuel, A. D. (2011). Optogenetic manipulation of neural activity in freely moving *Caenorhabditis elegans*. *Nat Methods*, 8(2), 147-152. doi:10.1038/nmeth.1554
- Li, Z., Liu, J., Zheng, M., & Xu, X. Z. (2014). Encoding of both analog- and digital-like behavioral outputs by one *C. elegans* interneuron. *Cell*, 159(4), 751-765. doi:10.1016/j.cell.2014.09.056
- Lindsay, T. H., Thiele, T. R., & Lockery, S. R. (2011). Optogenetic analysis of synaptic transmission in the central nervous system of the nematode *Caenorhabditis elegans*. *Nat Commun*, 2, 306. doi:10.1038/ncomms1304
- Liu, M., Sharma, A. K., Shaevitz, J. W., & Leifer, A. M. (2018). Temporal processing and context dependency in *Caenorhabditis elegans* response to mechanosensation. *Elife*, 7. doi:10.7554/eLife.36419
- Liu, P., Chen, B., Altun, Z. F., Gross, M. J., Shan, A., Schuman, B., . . . Wang, Z. W. (2013). Six innexins contribute to electrical coupling of *C. elegans* body-wall muscle. *PLoS One*, 8(10), e76877. doi:10.1371/journal.pone.0076877
- Long, M. A., Jin, D. Z., & Fee, M. S. (2010). Support for a synaptic chain model of neuronal sequence generation. *Nature*, 468(7322), 394-399. doi:10.1038/nature09514
- Louie, K., & Wilson, M. A. (2001). Temporally structured replay of awake hippocampal ensemble activity during rapid eye movement sleep. *Neuron*, 29(1), 145-156. doi:10.1016/s0896-6273(01)00186-6
- Luo, L., Wen, Q., Ren, J., Hendricks, M., Gershow, M., Qin, Y., . . . Zhang, Y. (2014). Dynamic encoding of perception, memory, and movement in a *C. elegans* chemotaxis circuit. *Neuron*, 82(5), 1115-1128. doi:10.1016/j.neuron.2014.05.010
- Mainen, Z. F., & Sejnowski, T. J. (1995). Reliability of spike timing in neocortical neurons. *Science*, 268(5216), 1503-1506. doi:10.1126/science.7770778
- Marvin, J. S., Borghuis, B. G., Tian, L., Cichon, J., Harnett, M. T., Akerboom, J., . . . Looger, L. L. (2013). An optimized fluorescent probe for visualizing glutamate neurotransmission. *Nat Methods*, 10(2), 162-170. doi:10.1038/nmeth.2333
- Mastrogiuseppe, F., & Ostojic, S. (2018). Linking Connectivity, Dynamics, and Computations in Low-Rank Recurrent Neural Networks. *Neuron*, 99(3), 609-623 e629. doi:10.1016/j.neuron.2018.07.003
- Mohammadi, A., Byrne Rodgers, J., Kotera, I., & Ryu, W. S. (2013). Behavioral response of *Caenorhabditis elegans* to localized thermal stimuli. *BMC Neurosci*, 14(1), 66. doi:10.1186/1471-2202-14-66
- Mori, I., & Ohshima, Y. (1995). Neural regulation of thermotaxis in *Caenorhabditis elegans*. *Nature*, 376(6538), 344-348. doi:10.1038/376344a0
- Nagel, G., Brauner, M., Liewald, J. F., Adeishvili, N., Bamberg, E., & Gottschalk, A. (2005). Light activation of channelrhodopsin-2 in excitable cells of *Caenorhabditis elegans* triggers rapid behavioral responses. *Curr Biol*, 15(24), 2279-2284. doi:10.1016/j.cub.2005.11.032

- Narayan, A., Laurent, G., & Sternberg, P. W. (2011). Transfer characteristics of a thermosensory synapse in *Caenorhabditis elegans*. *Proc Natl Acad Sci U S A*, 108(23), 9667-9672. doi:10.1073/pnas.1106617108
- Nguyen, J. P., Shipley, F. B., Linder, A. N., Plummer, G. S., Liu, M., Setru, S. U., . . . Leifer, A. M. (2016). Whole-brain calcium imaging with cellular resolution in freely behaving *Caenorhabditis elegans*. *Proc Natl Acad Sci U S A*, 113(8), E1074-1081. doi:10.1073/pnas.1507110112
- Pierce-Shimomura, J. T., Morse, T. M., & Lockery, S. R. (1999). The fundamental role of pirouettes in *Caenorhabditis elegans* chemotaxis. *J Neurosci*, 19(21), 9557-9569.
- Pirri, J. K., McPherson, A. D., Donnelly, J. L., Francis, M. M., & Alkema, M. J. (2009). A tyramine-gated chloride channel coordinates distinct motor programs of a *Caenorhabditis elegans* escape response. *Neuron*, 62(4), 526-538. doi:10.1016/j.neuron.2009.04.013
- Pokala, N., Liu, Q., Gordus, A., & Bargmann, C. I. (2014). Inducible and titratable silencing of *Caenorhabditis elegans* neurons in vivo with histamine-gated chloride channels. *Proc Natl Acad Sci U S A*, 111(7), 2770-2775. doi:10.1073/pnas.1400615111
- Qi, Y. B., Garren, E. J., Shu, X., Tsien, R. Y., & Jin, Y. (2012). Photo-inducible cell ablation in *Caenorhabditis elegans* using the genetically encoded singlet oxygen generating protein miniSOG. *Proc Natl Acad Sci U S A*, 109(19), 7499-7504. doi:10.1073/pnas.1204096109
- Rajan, K., Harvey, C. D., & Tank, D. W. (2016). Recurrent Network Models of Sequence Generation and Memory. *Neuron*, 90(1), 128-142. doi:10.1016/j.neuron.2016.02.009
- Remington, E. D., Egger, S. W., Narain, D., Wang, J., & Jazayeri, M. (2018). A Dynamical Systems Perspective on Flexible Motor Timing. *Trends Cogn Sci*, 22(10), 938-952. doi:10.1016/j.tics.2018.07.010
- Remington, E. D., Narain, D., Hosseini, E. A., & Jazayeri, M. (2018). Flexible Sensorimotor Computations through Rapid Reconfiguration of Cortical Dynamics. *Neuron*, 98(5), 1005-1019 e1005. doi:10.1016/j.neuron.2018.05.020
- Roberts, W. M., Augustine, S. B., Lawton, K. J., Lindsay, T. H., Thiele, T. R., Izquierdo, E. J., . . . Lockery, S. R. (2016). A stochastic neuronal model predicts random search behaviors at multiple spatial scales in *C. elegans*. *Elife*, 5. doi:10.7554/eLife.12572
- Seeds, A. M., Ravbar, P., Chung, P., Hampel, S., Midgley, F. M., Jr., Mensh, B. D., & Simpson, J. H. (2014). A suppression hierarchy among competing motor programs drives sequential grooming in *Drosophila*. *Elife*, 3, e02951. doi:10.7554/eLife.02951
- Serrano-Saiz, E., Poole, R. J., Felton, T., Zhang, F., De La Cruz, E. D., & Hobert, O. (2013). Modular control of glutamatergic neuronal identity in *C. elegans* by distinct homeodomain proteins. *Cell*, 155(3), 659-673. doi:10.1016/j.cell.2013.09.052
- Shmiel, T., Drori, R., Shmiel, O., Ben-Shaul, Y., Nadasdy, Z., Shemesh, M., . . . Abeles, M. (2006). Temporally precise cortical firing patterns are associated with distinct action segments. *J Neurophysiol*, 96(5), 2645-2652. doi:10.1152/jn.00798.2005
- Skaggs, W. E., & McNaughton, B. L. (1996). Replay of neuronal firing sequences in rat hippocampus during sleep following spatial experience. *Science*, 271(5257), 1870-1873. doi:10.1126/science.271.5257.1870
- Starich, T. A., Herman, R. K., & Shaw, J. E. (1993). Molecular and genetic analysis of *unc-7*, a *Caenorhabditis elegans* gene required for coordinated locomotion. *Genetics*, 133(3), 527-541.
- Starich, T. A., Xu, J., Skerrett, I. M., Nicholson, B. J., & Shaw, J. E. J. N. d. (2009). Interactions between innexins UNC-7 and UNC-9 mediate electrical synapse specificity in the *Caenorhabditis elegans* locomotory nervous system. *Neural development*, 4(1), 16.
- Stephens, G. J., Bueno de Mesquita, M., Ryu, W. S., & Bialek, W. (2011). Emergence of long timescales and stereotyped behaviors in *Caenorhabditis elegans*. *Proc Natl Acad Sci U S A*, 108(18), 7286-7289. doi:10.1073/pnas.1007868108
- Stephens, G. J., Johnson-Kerner, B., Bialek, W., & Ryu, W. S. (2008). Dimensionality and dynamics in the behavior of *C. elegans*. *PLoS Comput Biol*, 4(4), e1000028. doi:10.1371/journal.pcbi.1000028

- Sutton, R. S., & Barto, A. G. (2017). *Reinforcement Learning: An Introduction*. . Cambridge, MA: MIT Press.
- Tumer, E. C., & Brainard, M. S. (2007). Performance variability enables adaptive plasticity of 'crystallized' adult birdsong. *Nature*, 450(7173), 1240-1244. doi:10.1038/nature06390
- van Vreeswijk, C., & Sompolinsky, H. (1996). Chaos in neuronal networks with balanced excitatory and inhibitory activity. *Science*, 274(5293), 1724-1726. doi:10.1126/science.274.5293.1724
- Venkatachalam, V., Ji, N., Wang, X., Clark, C., Mitchell, J. K., Klein, M., . . . Samuel, A. D. (2016). Pan-neuronal imaging in roaming *Caenorhabditis elegans*. *Proc Natl Acad Sci U S A*, 113(8), E1082-1088. doi:10.1073/pnas.1507109113
- White, J. G., Southgate, E., Thomson, J. N., & Brenner, S. (1986). The structure of the nervous system of the nematode *Caenorhabditis elegans*. *Philos Trans R Soc Lond B Biol Sci*, 314(1165), 1-340. doi:10.1098/rstb.1986.0056
- Wicks, S. R., Roehrig, C. J., & Rankin, C. H. (1996). A dynamic network simulation of the nematode tap withdrawal circuit: predictions concerning synaptic function using behavioral criteria. *J Neurosci*, 16(12), 4017-4031.
- Witvliet, D., Mulcahy, B., Mitchell, J. K., Meirovitch, Y., Berger, D. K., Wu, Y., . . . Holmyard, D. J. b. (2020). Connectomes across development reveal principles of brain maturation in *C. elegans*. *bioRxiv*.
- Xu, S., & Chisholm, A. D. (2016). Highly efficient optogenetic cell ablation in *C. elegans* using membrane-targeted miniSOG. *Sci Rep*, 6, 21271. doi:10.1038/srep21271
- Xu, T., Huo, J., Shao, S., Po, M., Kawano, T., Lu, Y., . . . Wen, Q. (2018). Descending pathway facilitates undulatory wave propagation in *Caenorhabditis elegans* through gap junctions. *Proc Natl Acad Sci U S A*, 115(19), E4493-E4502. doi:10.1073/pnas.1717022115

Appendix

This note provides a theoretical account of the time-dependent type-II (RT) transition rate. First, we shall consider how type-II transition arises through a rapid change of neuronal activity, represented experimentally by inter/motor neurons RIV. Second, we shall argue that the introduction of short-term synaptic depression (STD) in the inhibitory synapses may provide an explanation of the type-II transition rate.

A biophysical model

Consider a model neuron (e.g. RIV) in the turning module receiving excitatory inputs through gap junction and inhibitory inputs through synapses (**Figure 7A**). The following equation describes the membrane potential x of a neuron determined by the gap junction conductance, inhibitory synaptic conductance and leaky conductance, represented by G^g , G^i and G^c respectively (Varshney, Chen, Paniagua, Hall, & Chklovskii, 2011).

$$C\dot{x} = -G^g(x - E^e) - G^i(x - E^i) - G^c(x - E^c) + I^{Noise} \quad (1.1)$$

Since the excitatory gap junction input is from AIB, here we use E^e to represent the voltage of AIB in the first term. E^i and E^c denote the reversal potential of inhibitory synapse and the resting potential. I^{noise} is Gaussian white noise, which could be regarded as the fluctuation of synaptic currents and other sources of noises that are not explicitly considered in the model.

For simplicity, let us first assume that all the inputs, G^g , G^i and G^c , are constants. This assumption will be relaxed later when we introduce short-term synaptic plasticity in inhibitory synapses, with which G^i decreases while G^g and G^c remain unchanged. E^e , the membrane

potential of AIB is treated as a constant, provided that the backward module exhibits persistent activity during a reversal. The fixed point x_0 is given by

$$x_0 = \frac{E^e G^g + E^i G^i + E^c G^c}{G^g + G^i + G^c} = (\dot{a}_m E^m G^m) / \dot{a}_m G^m \quad (1.2)$$

where m denotes all kinds of inputs, including gap junctions, chemical synapses and leaky channels.

G^m and E^m are the conductance of an input and the corresponding target voltage.

With small perturbation $x_0 \rightarrow x_0 + Dx$, we make an approximation

$$C\dot{x} = -\sum_m G^m \cdot \Delta x, \quad (1.3)$$

provided that the synaptic inputs from other neurons are insensitive to small fluctuation of the membrane potential of a postsynaptic neuron. In this case, the membrane potential can be viewed as a one-dimensional Brownian particle which obeys the following equation

$$\dot{x} = -k(x - x_0) + \eta, x < x_{th} \quad (1.4)$$

where $k = \sum_m G^m / C$, and η is gaussian white noise. To capture the essential process of type-II transition, we assume that the membrane potential x fluctuates around x_0 during a reversal. Once the noise drives the membrane potential across a threshold x_{th} , the system transitions to a different state: RIV neurons become rapidly depolarized due to a nonlinear rectified activation (**Figure 3E** and **Figure 7B**), starting a turn by activating ventral muscles and terminating the reversal via feedback inhibition (**Figure 7A** and **7D**).

Calculating the stationary probability density near fixed point with Fokker-Plank equation

835 Fokker-Planck equation that describes the probability density of the particle position (Hänggi,
836 Talkner, & Borkovec, 1990) is

$$837 \quad \frac{\partial P(x,t)}{\partial t} = \frac{\partial}{\partial x} [-k(x-x_0)P(x,t)] + \sigma^2 \frac{\partial^2 P(x,t)}{\partial x^2} \quad (2.1)$$

838 where σ determines the amplitude of noise. According to Einstein's theory on Brownian motion,
839 σ and the variance of Gaussian white noise η has the following relation:

$$840 \quad \sigma^2 = \frac{\Delta t}{2} \langle \eta^2 \rangle \quad (2.2)$$

841 where Δt is the time step.

842 The stationary solution for Fokker-Planck equation $\frac{\partial P(x,t)}{\partial t} = 0$ is given by:

$$843 \quad P(x) \sim e^{-\frac{k(x-x_0)^2}{2\sigma^2}} \quad (2.3)$$

844 which is similar to Boltzmann distribution, where $\frac{k(x-x_0)^2}{2}$ can be viewed as the potential
845 energy $U(x)$, and σ^2 plays the role of temperature $k_B T$.

846 **Biophysical understanding of the type-II transition**

847 Now consider a terminal threshold x_{th} , beyond which the system transits to a different state.
848 Assuming that the barrier is high and the particle is restricted in the energy well, we shall next
849 calculate the small, albeit not negligible probability current J crossing the barrier.

850 From Fokker-Planck equation (2.1) we have:

$$\begin{aligned}
\frac{\partial P(x,t)}{\partial t} &= \frac{\partial}{\partial x} [k(x-x_0)P(x,t)] + \sigma^2 \frac{\partial^2 P(x,t)}{\partial x^2} \\
&= \frac{\partial}{\partial x} [k(x-x_0)P(x,t) + \sigma^2 \frac{\partial P(x,t)}{\partial x}] \\
&= -\frac{\partial J(x,t)}{\partial x}
\end{aligned} \tag{3.1}$$

Current J can be rewritten in another form

$$J(x,t) = -\sigma^2 e^{-\frac{k(x-x_0)^2}{2\sigma^2}} \frac{\partial}{\partial x} [e^{\frac{k(x-x_0)^2}{2\sigma^2}} P(x,t)] \tag{3.2}$$

Considering a stationary state, we have $\frac{\partial P(x,t)}{\partial t} \approx 0$, $J \approx \text{const}$

$$\frac{\partial}{\partial x} [e^{\frac{k(x-x_0)^2}{2\sigma^2}} P(x)] = -\frac{J}{\sigma^2} e^{\frac{k(x-x_0)^2}{2\sigma^2}} \tag{3.3}$$

Integrate Eq. (3.3) between x_0 and x_{th}

$$[e^{\frac{k(x-x_0)^2}{2\sigma^2}} P(x)] \Big|_{x_0}^{x_{th}} = -\frac{J}{\sigma^2} \int_{x_0}^{x_{th}} e^{\frac{k(x-x_0)^2}{2\sigma^2}} dx \tag{3.4}$$

Since the particle is restricted around x_0 , $P(x_{th}) \approx 0$, then we have

$$J = \frac{\sigma^2 P(x_0)}{\int_{x_0}^{x_{th}} e^{\frac{k(x-x_0)^2}{2\sigma^2}} dx} \tag{3.5}$$

To get $P(x_0)$ in Eq. (3.5), note that the probability of finding the particle around x_0 should

be 1, and $P(x) = P(x_0) e^{-\frac{k(x-x_0)^2}{2\sigma^2}}$ according to Eq. (2.3), we have

$$P(x_0) \int_{-\infty}^{+\infty} e^{-\frac{k(x-x_0)^2}{2\sigma^2}} dx = 1 \quad (3.6)$$

Let A denote $\sqrt{\frac{k}{2\sigma^2}}$

$$P(x_0) \int_{x_0-h}^{x_0+h} e^{-\frac{k(x-x_0)^2}{2\sigma^2}} dx = P(x_0) \int_{-h}^h e^{-(Ax)^2} dx = P(x_0) \frac{\sqrt{\pi}}{A} \operatorname{erf}(Ah) = 1 \quad (3.7)$$

where $\operatorname{erf}(x) = \frac{2}{\sqrt{\pi}} \int_0^x e^{-z^2} dz$ is the error function.

By taking the limit $h \rightarrow +\infty$, $\operatorname{erf}(Ah) \rightarrow 1$, we find

$$P(x_0) = \frac{A}{\sqrt{\pi}} \quad (3.8)$$

The denominator $\int_{x_0}^{x_{th}} e^{-\frac{k(x-x_0)^2}{2\sigma^2}} dx$ in Eq. (3.5) can be calculated directly

$$\int_{x_0}^{x_{th}} e^{-\frac{k(x-x_0)^2}{2\sigma^2}} dx = \int_0^{x_{th}-x_0} e^{-(Ax)^2} dx = \frac{\sqrt{\pi}}{2A} \operatorname{erfi}(A(x_{th}-x_0)) \quad (3.9)$$

where $\operatorname{erfi}(x) = \frac{2}{\sqrt{\pi}} \int_0^x e^{z^2} dz$ is imaginary error function

Substituting Eqs. (3.8)- (3.9) into Eq. (3.5), we finally obtain the transition rate r

$$r = J = \frac{k}{\pi} \cdot \operatorname{erfi}^{-1}\left(\sqrt{\frac{k}{2\sigma^2}}(x_{th}-x_0)\right) \quad (3.10)$$

Transition rate with short-term synaptic depression

Since the membrane time constant of a neuron (~ 10 ms) is much smaller than the behavioral timescale (\sim s), the probability density approaches the stationary state rapidly and Eq. (3.10) is a constant rather than a function of time, resulting in an exponential distribution of the dwell time. To explain the time-dependent type-II transition rate (**Figure 1C-D**), we introduce plasticity in the inhibitory synapses, analogous to short-term synaptic depression (STD).

As the inhibition onto the model neuron becomes weaker, fixed point x_0 moves towards threshold x_{th} ; k , which characterizes the steepness of the potential energy, becomes shallower. Both analytical calculation and simulation suggest that the change of x_0 has a much larger effect on the transition rate in the region $x_{th} - x_0 \ll E^e - E^i$, where E^e or E^i is the reversal potential for excitatory or inhibitory synapses.

In this regime, consider a simple case when x_0 varies with time for a fixed k . Assuming the strength of synaptic inhibition decreases exponentially, we have

$$\begin{aligned} r_2(t) &= \frac{k}{\rho} \times \text{erfi}^{-1} \left(\sqrt{\frac{k}{2S^2}} (x_{th} - x_0(t)) \right) \\ &= \frac{k}{\rho} \times \text{erfi}^{-1} \left(\sqrt{\frac{k}{2S^2}} (x_{th} - x_{fin} + (x_{fin} - x_{ini})e^{(-t/t)}) \right) \\ &= k_1 \times \text{erfi}^{-1} (k_2 + k_3 e^{(-t/t)}) \end{aligned} \quad (4.1)$$

Eq. (4.1) was used to fit the type-II transition rate.

References

- Hänggi, P., Talkner, P., & Borkovec, M. (1990). Reaction-rate theory: fifty years after Kramers. *Reviews of Modern Physics*, 62(2), 251-341. doi:10.1103/RevModPhys.62.251
- Varshney, L. R., Chen, B. L., Paniagua, E., Hall, D. H., & Chklovskii, D. B. (2011). Structural properties of the *Caenorhabditis elegans* neuronal network. *PLoS Comput Biol*, 7(2), e1001066. doi:10.1371/journal.pcbi.1001066

Figure legends

Figure 1. Flexible motor sequence generation during *C. elegans* escape responses. **(A)** Optogenetic stimulation of mechanosensory neurons ALM/AVM (*Pmec-4::ChR2*) was carried out with blue light (473 nm, 4.63 mW/mm²) for 1.5 s during animal forward movement. Identical stimuli could induce four different behavioral outputs: reversal followed by an omega turn, reversal followed by forward movement, pause state or forward movement (no response). **(B)** Definition of type-I and type-II transitions. **(C)** Reversal length distribution (left) and transition rates (right) during ALM/AVM (*Pmec-4::ChR2*) triggered escape responses. Total number of trials, $n=674$; reversal without turn, $n=272$; reversal with turn, $n=322$; no response, $n=79$; pause, $n=1$. Here and below, the error bars of transition rates represent 95% binomial proportion confidence interval. **(D)** Reversal length distribution (left) and transition rates (right) during thermal stimulus induced escape responses. Wild-type, $n=385$. Animal heads were thermally stimulated by an infrared laser (1480 nm; 400 mA) for 0.75 s. Solid lines are theoretical fits using Eq. (4) and fitted type-II transition rates pass goodness-of-fit test ($p>0.05$).

The online version of this article includes the following figure supplement(s) for figure 1:

Figure 1—figure supplement 1. Definition of the type II transition and statistical test of reversal length distribution.

Figure 2. Interneurons AIB are crucial for motor state transitions. **(A)** Simplified circuit diagram underlying the gentle touch induced escape responses. Neurons were grouped into four modules based on their functional roles and activity patterns. **(B)** Calcium activity of AIB during

spontaneous reversals before type-I ($n=23$) and type-II ($n=36$) transitions in unrestrained behaving animals (*Pinx-I::GCaMP6;Pinx-I::wCherry*). Here, data are aligned to the ends of reversals (vertical dashed line, $t = 0$). Heat map across trials (up) and $\Delta R(t)/R_0$ (Mean \pm SEM, bottom) are shown. (C) Ramping rate of calcium activity in AIB. Up, raw single trial $\Delta R(t)/R_0$ from reversal start to reversal end. The ramping rate is the slope of the red line, fitted by linear regression. Bottom, ramping rates of AIB during type-I and type-II transitions. Each color (Mean \pm SEM) represents single animal data across multiple trials. Total 9 animals (*Pinx-I::GCaMP6;Pinx-I::wCherry*) were tested. Very short reversals (less than 1.5 s) are excluded, for some of them have negative ramping rates and the slope estimate is susceptible to noise (but including those trials doesn't affect our conclusion). ** $p < 0.01$, two-way ANOVA. (D) Optogenetic activation of AIB (635 nm, 4.46 mW/mm², 7 s) or inhibition of AIB (561nm, 21.71 mW/mm², 12 s) during ALM/AVM (473 nm, 14.71 mW/mm², 1.5 s) triggered avoidance behaviors, reversal durations (bar graph) and fractions of animals executing omega turns (pie chart) are shown. Error bars are SEMs. Bar graph, Mann–Whitney U test. Pie chart, χ^2 test. * $p < 0.05$, *** $p < 0.001$, **** $p < 0.0001$. Here and below, the actual turning percentages ($n_{\text{turn}}/n_{\text{total}}$) are noted beside the pie chart and numbers within the bars indicate trial number n . (E–F) Reversal length distribution (E) and transition rates (F) during escape responses when AIB were persistently hyperpolarized through an exogenous expression of the potassium channel TWK-18. Control group is from Figure 1C.

The online version of this article includes the following figure supplement(s) for figure 2:

Figure 2—figure supplement 1. Local interneurons AIB and RIM in the backward module differentially modulate motor state transitions.

Figure 3. Feedforward excitation via electrical coupling drives omega turns. **(A)** Calcium activity of RIV during the type-I ($n=38$) and the type-II ($n=18$) transitions in spontaneous behaving animals (*Plim-4::GCaMP6*). Here, data are aligned to the ends of reversals (vertical dashed line, $t = 0$). Heat map across trials (left) and $\Delta F(t)$ (Mean \pm SEM, right) are shown. **(B)** Optical neurophysiology for probing the feedforward coupling between the backward module and the turning module. **(C)** Simultaneous optogenetic activation of AIB (635nm, 6.11 mW/mm²) and calcium imaging of RIV in immobilized animals. $\Delta R(t)/R_0$ (Mean \pm SEM) under different genetic backgrounds are shown: control (ATR) is wild-type (dark blue); *inx-1 unc-9 unc-7* triple mutant (red); calcium imaging of RIV in the presence of moderate inhibition (561 nm, 1.94 mW/mm²) of RIV (light blue, *Plim-4::Arch*). The control (no ATR) represents imaging data from wild-type animals without feeding all-trans retinal (grey). **** $p < 0.0001$, two-way ANOVA. **(D)** Probability of a reversal followed by a turn (left) and type-II transition rates (right) for gap junction deficient mutants. AIB, expressing Chrimson, were optogenetically activated for 7 s (635 nm, 4.46 mW/mm²) in wild-type animals (green), gap junction deficient mutants *inx-1* (red), and *inx-1* mutants, in which INX-1 channels were restored specifically in AIB (blue). Error bars indicate 95% binomial proportion confidence interval. χ^2 test. **** $p < 0.0001$. **(E)** Simultaneous optogenetic activation of AIB (635nm, 6.11 mW/mm²) and calcium imaging of RIV in unrestrained behaving animals. Left, calcium activity heatmap across trials. $t < 0$ represents reversals. Omega turns start at $t = 0$. Right, $\Delta F(t)$ (mean \pm SEM) are shown (blue). **(F)** Data are related to Figure 3E, but $t = 0$ is aligned to the beginning of AIB stimulation.

The online version of this article includes the following figure supplement(s) for figure 3:

Figure 3—figure supplement 1. Optogenetic activation of AIB and calcium imaging of RIV in different experimental conditions.

Figure 3—figure supplement 2. Possible polysynaptic pathways from AIB to RIV (less than four layers are shown) according to *C. elegans* connectome.

Figure 4. Glutamatergic inhibition modulates type-II transition. **(A)** Reversal durations (left) and type-II transition rates (right) in glutamatergic synaptic transmission deficient animals upon strong and persistent optogenetic activation of AIB. Optogenetic stimulation was delivered for 7 s using red light (635 nm, 4.46 mW/mm²). Right, compare r_2 in *eat-4* mutant or in *Pnpr-9::TeTx* with control animals across the whole distribution (Kolmogorov-Smirnov test, $p=6.2e-7$, $p=0.0026$) or within a time window (χ^2 test: * $p<0.05$, ** $p<0.01$, *** $p<0.001$, **** $p<0.0001$). **(B)** Reversal durations (left) and type-II transition rates (right) in GluCl receptor mutants upon optogenetic activation of AIB (635 nm, 4.46 mW/mm²). Right, compare r_2 in triple receptor mutant with control animals across the whole distribution (Kolmogorov-Smirnov test, $p=5.9e-8$) or within a time window (χ^2 test: * $p<0.05$, ** $p<0.01$). **(C)** Genes encoding GluCl receptors were expressed in local interneurons RIB and AIY respectively. GFP reporter lines were constructed using *avr-14*, *avr-15* and *glc-1* promoters, respectively; mCherry (or wCherry) reporters were used for cell identification. Expression pattern from one section is showed. Scale bar, 10 μ m. **(D)** Simultaneous optogenetic activation of AIB (635nm, 6.11 mW/mm²) and calcium imaging of RIB in immobilized animals under wide-type (control (ATR)) (blue) or *eat-4* glutamate deficient mutant background (red). $\Delta R(t)/R_0$ (Mean \pm SEM) are shown. $t = 0$ represents the beginning of AIB stimulation. The control group (no ATR) (grey) represents imaging data from animals without

feeding all-trans retinal. **** $p<0.0001$, two-way ANOVA. (E) Functional coupling between AIB and RIB neurons was directly tested through glutamate imaging. Upon stimulation of AIB (*Pnpr-9::Chrimson*), the process (red), cell body (green) of the RIB (*Psto-3::iGluSnFR*) and the RIB process in *eat-4* glutamate deficient mutants (grey) exhibited distinct fluorescence signals. The control group (blue) represents imaging data from animals without feeding all-trans retinal. Raw iGluSnFR imaging was recorded at 150 Hz. Trial average (bold color) and SEM (shaded region) are shown. Inset, the fluorescence signal of the process (red) is fitted with a double exponential function (blue), $B(e^{-\frac{t}{\tau_1}} - e^{-\frac{t}{\tau_2}}) + c$, where B , τ_1 , τ_2 and c are free parameters. τ_1 represents the time constant of glutamate signal decay, and c is the baseline constant, which was later subtracted in the inset plot.

For reversal duration, Error bars indicate SEM and Mann–Whitney U test. *** $p<0.001$, **** $p<0.0001$. All multiple comparisons were adjusted using Bonferroni correction.

The online version of this article includes the following figure supplement(s) for figure 4:

Figure 4—figure supplement 1. Glutamatergic inhibitions between AIB and RIB flexibly control the motor state transitions.

Figure 4—figure supplement 2. Functional coupling between AIB and RIB neurons was directly tested through glutamate imaging.

Figure 5. Local interneurons RIB promote both turning and forward behaviors. (A) Calcium activity of RIB during type-I (up, $n=41$) and type-II transitions (bottom, $n=25$). $\Delta F(t)$ (mean \pm SEM) are shown. $t = 0$ is aligned to the initiation of forward movement (up) or an omega turn

(bottom). **(B)** Statistics of motor state transitions (left) and representative curvature kymographs (right) upon optogenetic manipulation of RIB. Left, the probability for a transition and its 95% confidence limits were computed. RIB::Chrimson¹, $n=65$, red light (635 nm, 3.75 mW/mm²); RIB::Chrimson², $n=82$, red light (635 nm, 1.00 mW/mm²); RIB::Arch, $n=83$, green light (561 nm, 8.14 mW/mm²). Right, animals crawled on fresh agar plates. Body curvature was normalized by a $k \cdot L$, where L is the body length. Green (or red) shaded regions show selected spatiotemporal regions for optogenetic inhibition (or activation). The kymograph of turning behaviors exhibits longer cycles to complete body bending and larger body curvature, which are different from those during forward movements. **(C)** Reversal length distributions (left) and transition rates (right) when ALM/AVM activation was followed by optogenetic inhibition of RIB (12 s green light, 561 nm, 1.94 mW/mm²). *Pmec-4::ChR2;Psto-3::Arch*, $n=173$. Control group is from Figure 1C. **(D)** Calcium imaging of RIV in wild-type (blue) and RIB-ablated animals (orange) upon optogenetic stimulation of AIB in freely behaving animals. $\Delta R(t)/R_0$ (Mean \pm SEM) are shown. **(E)** Data are related to Figure 5D, but all trials are aligned to the onset of an omega turn. **(F)** Reversal length during ALM/AVM-triggered escape responses in RIB-ablated animals or in animals where chemical synaptic transmission from RIB was blocked. Error bars indicate SEM. Mann–Whitney U test, **** $p<0.0001$. All multiple comparisons were adjusted using Bonferroni correction.

The online version of this article includes the following figure supplement(s) for figure 5:

Figure 5—figure supplement 1. RIB receive feedforward inhibition to modulate type-II transition and neurons in the turning module might contribute to reversal termination.

Figure 6. Feedback inhibitions from the turning module contribute to reversal termination. **(A)** Expression pattern of *Plim-4::Arch::GFP*. Scale bar, 10 μm . **(B)** Left, escape responses induced by optogenetic activation of AIB (473 nm, 14.71 mW/mm², 1.5 s) or thermal stimulus (1480 nm, 0.75 s) followed by optogenetic inhibition of Arch-expressed interneurons (561nm, 21.71 mW/mm², 12 s). Bar graph, reversal durations, Mann–Whitney U test and error bars are SEMs. Pie chart, fractions of trials executing omega turns, χ^2 test. * $p < 0.05$, *** $p < 0.001$, **** $p < 0.0001$. All multiple comparisons were adjusted using Bonferroni correction. Right, schematic diagram for selective inhibition of RIV near animal head during thermally induced (1480 nm, 0.75 s) escape responses. **(C)** Up, reversal length distribution (left) and transition rate (right) in RIV/SAAD/SMB ablated animals. Bottom, spontaneous run length distribution (left) and transition rate from forward to backward movements (right) in wild-type animals. Insets are semiology plot of survival functions: proportion of trials moving backward (up) or forward (bottom) until t . We considered only trials with reversal duration ≥ 3 sec and forward duration ≥ 2 sec.

Figure 7. A model summary for motor sequence generation. **(A)** Schematics of neuronal circuit of *C. elegans* avoidance behavior. Feedforward excitations between local interneurons AIB and RIV trigger turning behavior. Glutamatergic inhibitions between AIB and RIB flexibly control the motor state transitions. Feedback inhibitions from the turning module help terminate backward behavior. **(B)** Illustration of the biophysical meaning of the type-II transition. The sub-threshold membrane potential of RIV fluctuates around the fixed point x_0 , just like a particle (red) in an energy well. When RIV membrane potential crosses the threshold x_{th} , RIV along with other neurons in the turning module become fully activated and a turn starts. **(C)** A simple stochastic attractor model without short-term synaptic plasticity cannot account for the experimentally

observed transition rate. **(D)** Schematics of a three-module model based on the animal connectome and experimentally identified functional motifs. Short-term synaptic depression (STD) was introduced in the feedforward inhibition. **(E)** Type-II transition rate during ALM/AVM triggered escape responses. Pink line is a theoretical fit using Eq. (4) and orange line is a fit using standard sigmoid function, both of which have three free parameters. τ_g in Eq. (4) is given by the glutamate decay time constant in **Figure 4E**, while τ in the standard sigmoid function is a free parameter.

Supplementary Figure legends

Figure 1—figure supplement 1. Definition of the type II transition and statistical test of reversal length distribution. (A) Left, examples of reorientation angle θ during the type-I (up) and the type-II transition (bottom). θ was measured as the angle between the head vector (BA) and the tail vector (DC). The worm body centerline was equally divided into 100 segments. The head vector (BA) is denoted as point B (mean coordinate of the 10th-14th segment) to A (mean coordinate of the 1st-5th segment), while the tail vector is denoted as point D (mean coordinate of 96th-100th segment) to C (mean coordinate of the 86th-90th segment). Immediately after the end of reversal, we identified a frame in which the worm exhibited a highly coiled body posture to calculate θ . If the head touched the body or tail, θ was computed from the frame before touching. Right, distribution of θ during ALM/AVM (*Pmec-4::ChR2*) triggered escape responses. A type-II transition was identified by either the head touching the body (or tail) or $\theta > 135^\circ$ within a single head swing. Total trials, $n=594$; type-I transition, $n=272$; type-II transition (touching the body or tail), $n=283$; type-II transition (no touching), $n=39$. (B) A Gaussian mixture model to fit the reversal length distribution during ALM/AVM (*Pmec-4::ChR2*) triggered escape responses. We performed the likelihood ratio test between the unimodal Gaussian distribution fit and the bimodal Gaussian mixture model fit. After computing the difference of the negative log likelihoods, we found a p -value = $5.4e-5$ using the χ_k^2 distribution, where $k = 3$ is the difference of the number of free parameters in the unimodal (total 2 parameters) and bimodal (total 5 parameters) distribution. At level $\alpha=0.01$, we have sufficient evidence that the bimodal distribution fits the reversal length better than the unimodal distribution.

Figure 2—figure supplement 1. Local interneurons AIB and RIM in the backward module differentially modulate motor state transitions. **(A)** The schematic diagram of *C. elegans* nervous system. **(B)** Multi-neuron calcium imaging in freely behaving animals (*Pnmr-1/ Plim-4/ Plgc-55/ Pnpr-9::NLS::wCherry::SL2::GCaMP6*). Interneurons in the backward and forward modules were simultaneously imaged using a confocal microscopy (see Materials and Methods for details). Data are aligned to the onset of a reversal (up, vertical dashed lines, $t = 0$) or the end of a turn (bottom, vertical dashed lines, $t = 0$). Heat map across trials and $\Delta R(t)/R_0$ (Mean \pm SEM) across trials are shown. **(C)** Ramping rate of AIB calcium activity during thermally-induced escape responses. Ramping rate is significantly higher in type-II transition (9 animals, each point has more than 3 trials). * $p < 0.05$, two-way ANOVA. **(D-E)** Characterization of the probability of type-II transition during optogenetic stimulation of two different interneurons AIB (left) and RIM (right) for varying durations. Longer activation of AIB consistently led to a higher probability of type-II transition (left). The control groups are animals performing spontaneous motor state transitions without optogenetic stimulation. A blue laser (473nm, 14.71 mW/mm²) was used to stimulate ChR2 expressed neurons. **(F-G)** Hyperpolarization of RIM (*Ptdc-1::Arch*) or AIB (*Pnpr-9::Arch*) both affected reversal duration (bar graph), but only inhibiting AIB affected the probability of type-II transition (pie chart). In **F**, simultaneous optogenetic activation of AIB (or RIM) (635nm, 4.46 mW/mm² for AIB or 473nm, 14.71 mW/mm² for RIM) and inhibition (561nm, 6.80 mW/mm²) of RIM (or AIB) were carried out for 7 (or 5) seconds. In **G**, RIM were activated for varying durations, while AIB were inactivated through an exogenous expression of the potassium channel TWK-18. **(H-I)** Reversal length distribution and transition rates after optogenetic ablation of AIB. ALM/AVM were optogenetically activated for 1.5 seconds to trigger avoidance behavior. AIB

were ablated by exogenous expression of a membrane targeted PH-miniSOG. Data from Figure 1C are used as control.

For reversal duration, error bars indicate SEMs. Mann–Whitney U test. For probability of turn, error bars indicate 95% binomial proportion confidence interval. χ^2 test. * $p<0.05$, ** $p<0.01$, *** $p<0.001$, **** $p<0.0001$. All multiple comparisons were adjusted using Bonferroni correction.

Figure 3—figure supplement 1. Optogenetic activation of AIB and calcium imaging of RIV in different experimental conditions. (A and C-F) Single trial data related to Figure 3A, C and E-F. In F, dashed lines indicate the start of a turn. (B) Calcium activity of RIV (*Plim-4::GCaMP6*, $n=20$) during thermal stimulus induced escape responses in freely moving animals. $\Delta\mathcal{R}(t) = [\Delta R(t) - \Delta R(t=0)]/R_0$ (mean \pm SEM) are shown. $t = 0$ is aligned to the initiation (up) or termination (bottom) of an omega turn.

Figure 3—figure supplement 2. Possible polysynaptic pathways from AIB to RIV (less than four layers are shown) according to *C. elegans* connectome. SDQ were oxygen-sensing neurons and topological cluster analyses suggest ADA may be involved in chemosensation. RIM, RIS and RIV have direct electrical coupling with AIB.

Figure 4—figure supplement 1. Glutamatergic inhibitions between AIB and RIB flexibly control the motor state transitions. (A) Couplings between the backward, forward and turning modules.

AIB, RIV and RIB are highlighted. **(B)** Reversal length during optogenetic activation of AIB in various glutamate postsynaptic receptor mutants and restoring *eat-4* specifically in AIB in different *eat-4* glutamate deficient mutants. GluCl single and double mutants exhibited longer reversals than the triple mutants (Figure 4B), suggesting that AVR-14, AVR-15 and GLC-1 proteins function synergistically to mediate feedforward inhibition. Error bars indicate SEMs. * $p < 0.05$, ** $p < 0.01$, **** $p < 0.0001$. Mann–Whitney U test. All multiple comparisons were adjusted using Bonferroni correction. **(C)** Single trial data related to Figure 4D.

Figure 4—figure supplement 2. Functional coupling between AIB and RIB neurons was directly tested through glutamate imaging. **(A)** Single trial data of the glutamatergic signal on the process of RIB after AIB activation onset, related to Figure 4E. Raw data and smoothed data (bold line) are showed. **(B)** Examination of AIB calcium activity after optogenetic activation of AIB, related to Figure 4E. Raw data and smoothed data (bold line) are showed.

Figure 5—figure supplement 1. RIB receive feedforward inhibition to modulate type-II transition and neurons in the turning module might contribute to reversal termination. **(A)** Single trial data related to Figure 5A. Dashed lines indicate the initiation of forward movement (up) or omega turns (bottom). **(B)** Persistent inhibition of RIB by expressing an exogenous histamine channel (HisCl) during ALM/AVM-triggered escape responses. Type-II transition quickly approached a plateau at a lower rate, which is consistent with our model prediction and Figure 5C. Control group is from Figure 1C. **(C)** Single trial data related to Figure 5D-E. **(D)** Left, simultaneous optogenetic activation of AIB and calcium imaging of RIV or SAAD/SMB (*Pnpr-9::Chrimson;Plim-*

1140 4::GCaMP6) in freely behaving animals. $t = 0$ is aligned to the onset of an omega turn. $\Delta F(t)$ (mean
1141 \pm SEM) are shown. Right, smoothed single trial data. Dashed lines indicate the start of a turn.
1142

1143 **Videos**

1144 Note that all videos were played at 0.625× speed. Blue/red *light on* indicates optogenetic excitation
1145 using blue/red light, while green *light on* indicates optogenetic inhibition using green light.

1146 **Video 1. Three main types of escape responses, Related to Figure 1.**

1147 Optogenetic activation of ALM/AVM mechanosensory neurons in freely moving worms for 1.5
1148 seconds induced three types of responses.

1149 **Video 2. AIB neurons are crucial for turn and backward movement, Related to Figure 2 and** 1150 **Figure 2—figure supplement 1.**

1151 Optogenetic activation of AIB neurons in free-moving animals reliably triggered backward
1152 movement followed by omega turns. Inhibition of AIB neurons quickly terminated backward
1153 movement.

1154 **Video 3. RIV neurons are essential for omega turns, Related to Figure 6.**

1155 Optogenetic ablation of RIV/SAA/SMB neurons abolished type-II transition, and animals could
1156 no longer generate a complete turn but executed a much longer reversal.

1157 **Video 4. Optogenetic activation of AIB under various genetic backgrounds, Related to Figure** 1158 **3 and Figure 4.**

1159 Optogenetic activation of AIB in *eat-4* glutamate vesicular transport deficient mutants or
1160 glutamate postsynaptic receptor mutants induced an omega turn preceded by a much shorter
1161 reversal. Specifically restoring *eat-4* in AIB or *glc-1* in AIY promoted a longer reversal. Activating
1162 AIB in gap junction deficient mutant *inx-1* reduced the probability of omega turn, which were
1163 rescued by restoring *inx-1* in AIB.

1164 **Video 5. Optogenetic manipulation of RIB can induce motor state transitions, Related to**
1165 **Figure 5.**

1166 Strong activation of RIB during forward movement reliably triggered turns; while inhibiting RIB
1167 during forward movement led to a pause state.

1168 **Video 6. Optogenetic inhibition of RIB or RIV/SAA/SMB neurons during escape responses**
1169 **prolonged reversal durations, Related to Figure 5 and Figure 6.**

1170

1171 **Supplementary Files**

1172 **Supplementary File 1. Strains information**

1173 **Supplementary File 2. Associated plasmids information**

1174 **Supplementary File 3. Associated promoter and gene information**

1175 **Supplementary File 4. Sample size and replicate number for all experiments**

1176

1177 **Source data**

1178 **Figure 1-source data 1**

1179 Source data for Figure 1 and Figure 1—figure supplement 1.

1180 **Figure 2-source data 1**

1181 Source data for Figure 2 and Figure 2—figure supplement 1.

1182 **Figure 3-source data 1**

1183 Source data for Figure 3.

1184 **Figure 4-source data 1**

1185 Source data for Figure 4 and Figure 4—figure supplement 1-2.

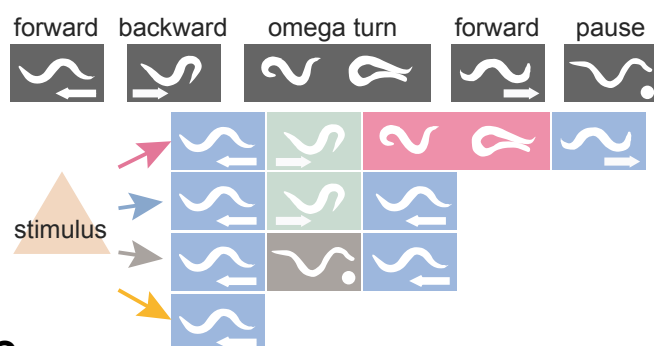
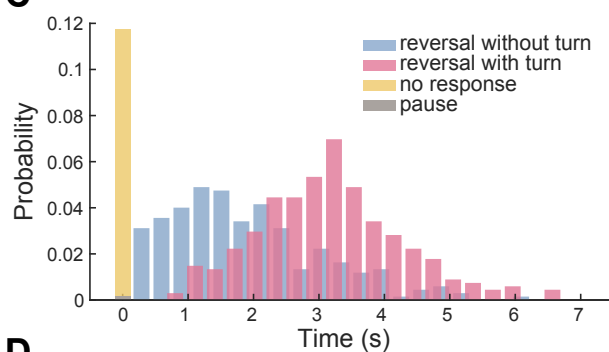
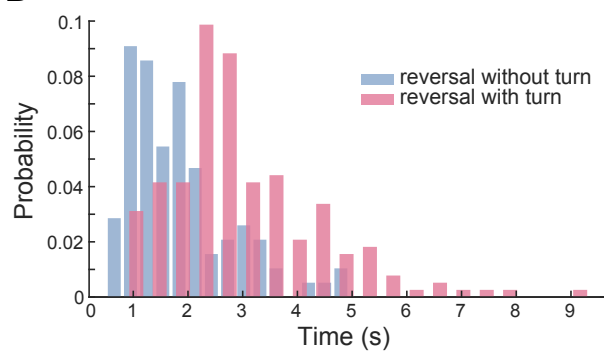
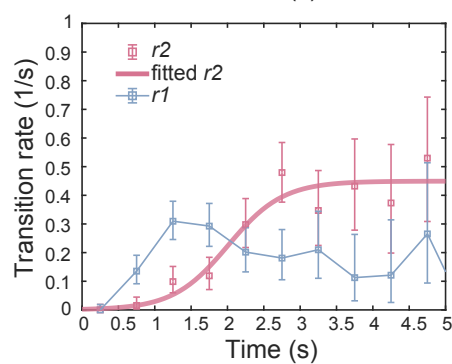
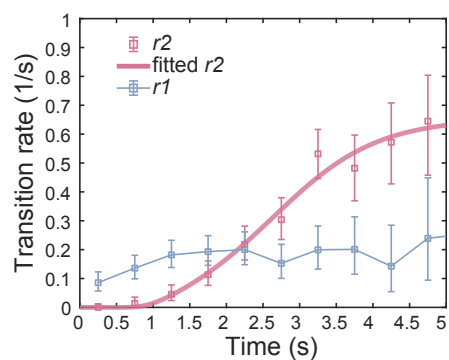
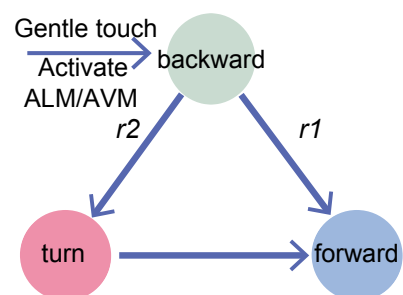
1186 **Figure 5-source data 1**

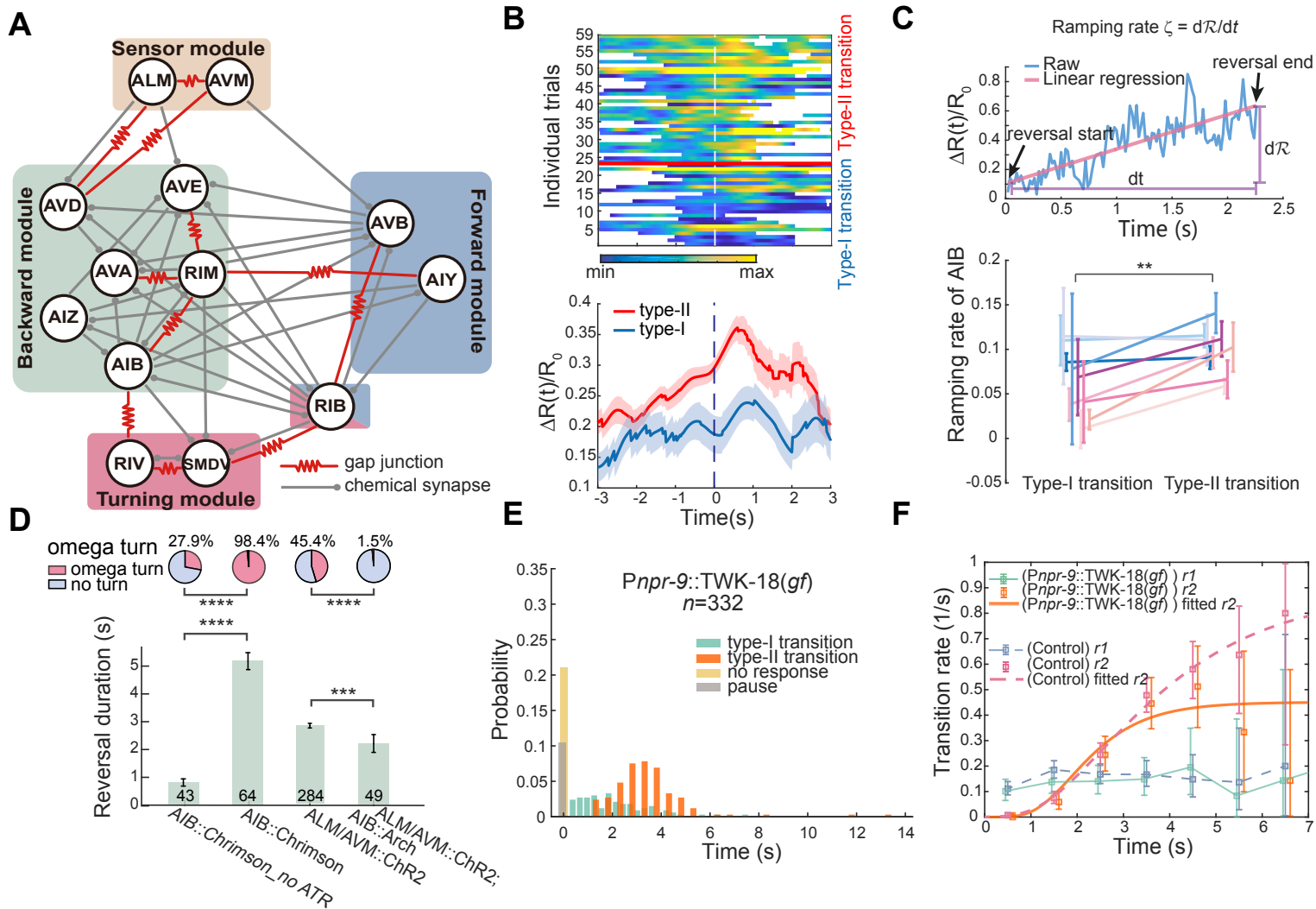
1187 Source data for Figure 5 and Figure 5—figure supplement 1.

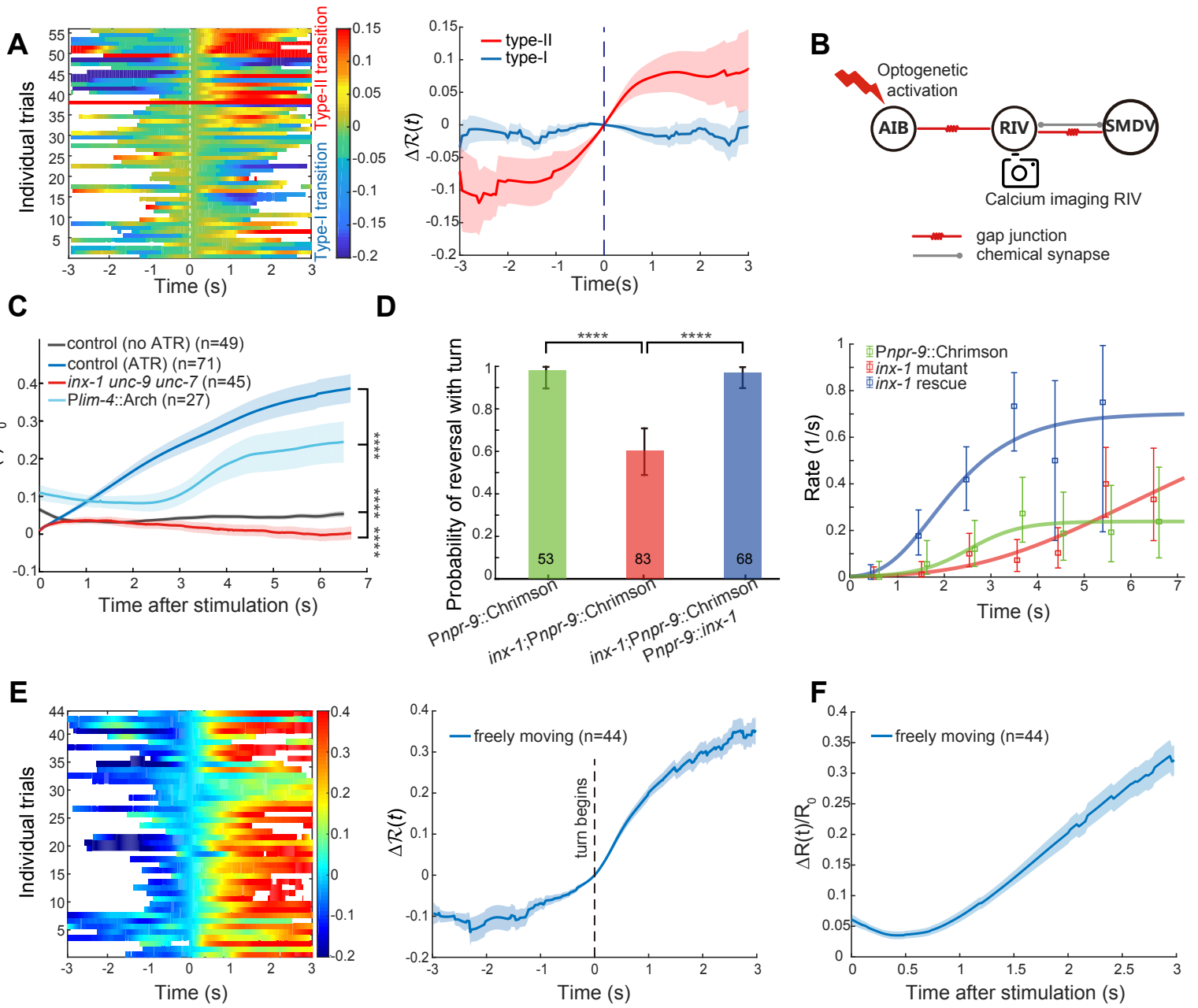
1188 **Figure 6-source data 1**

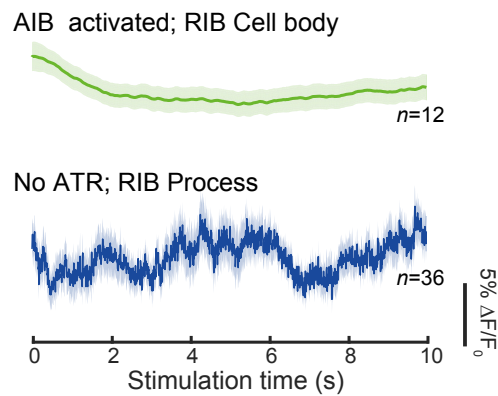
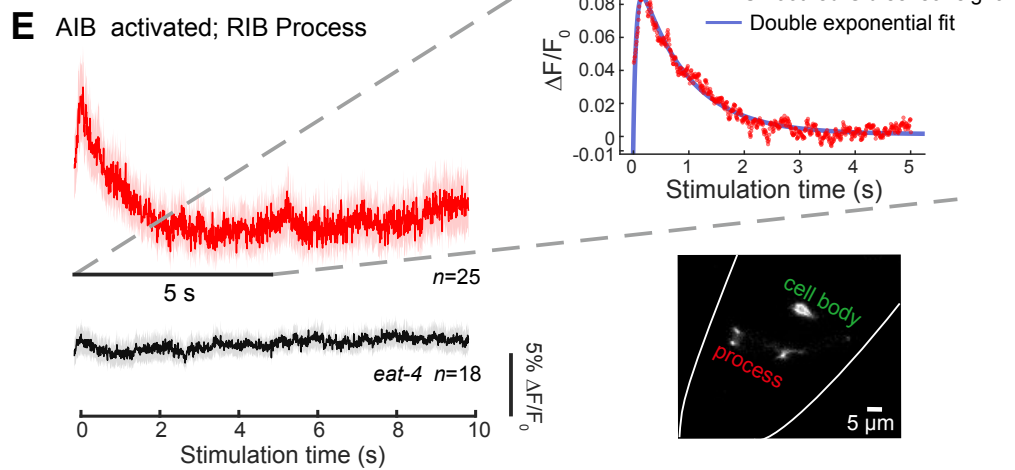
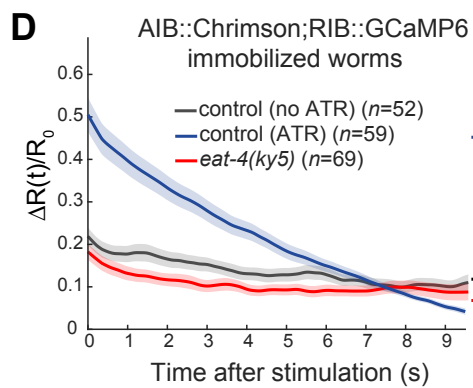
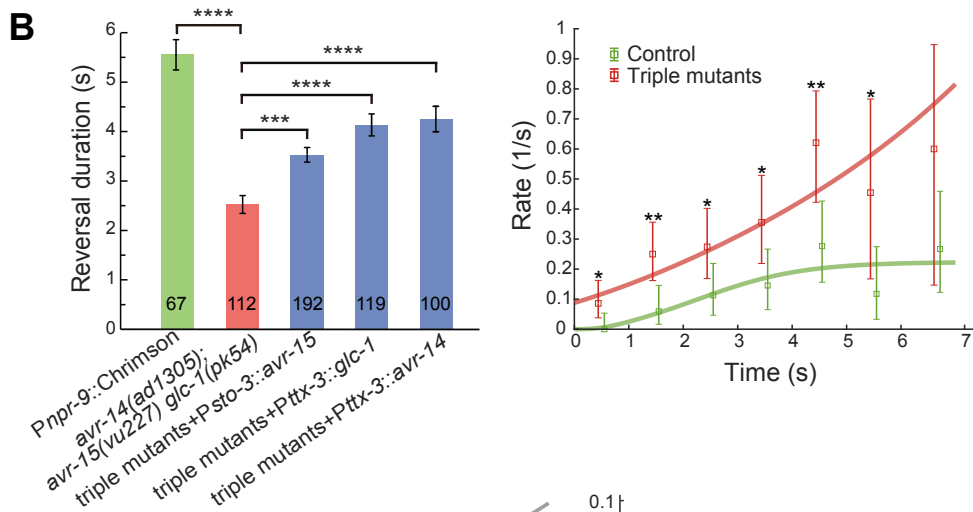
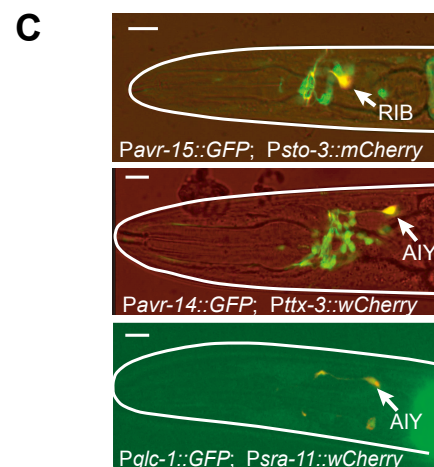
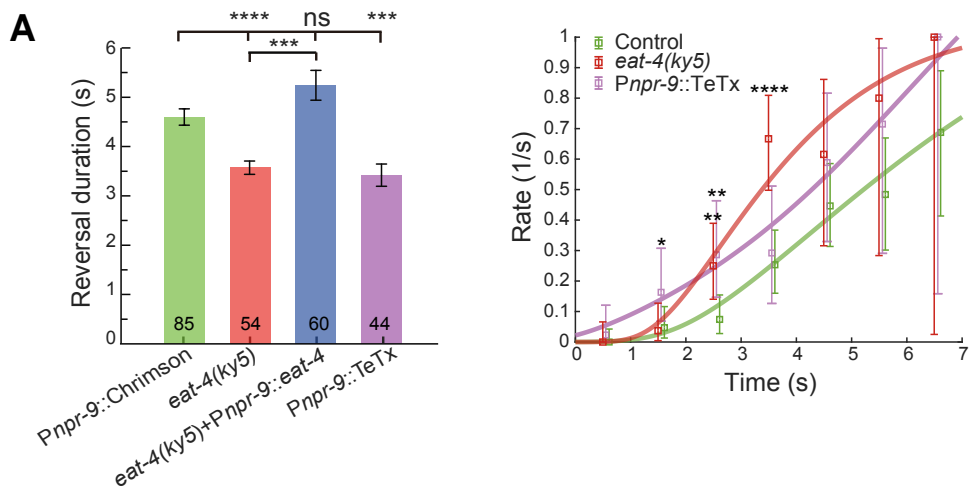
1189 Source data for Figure 6.

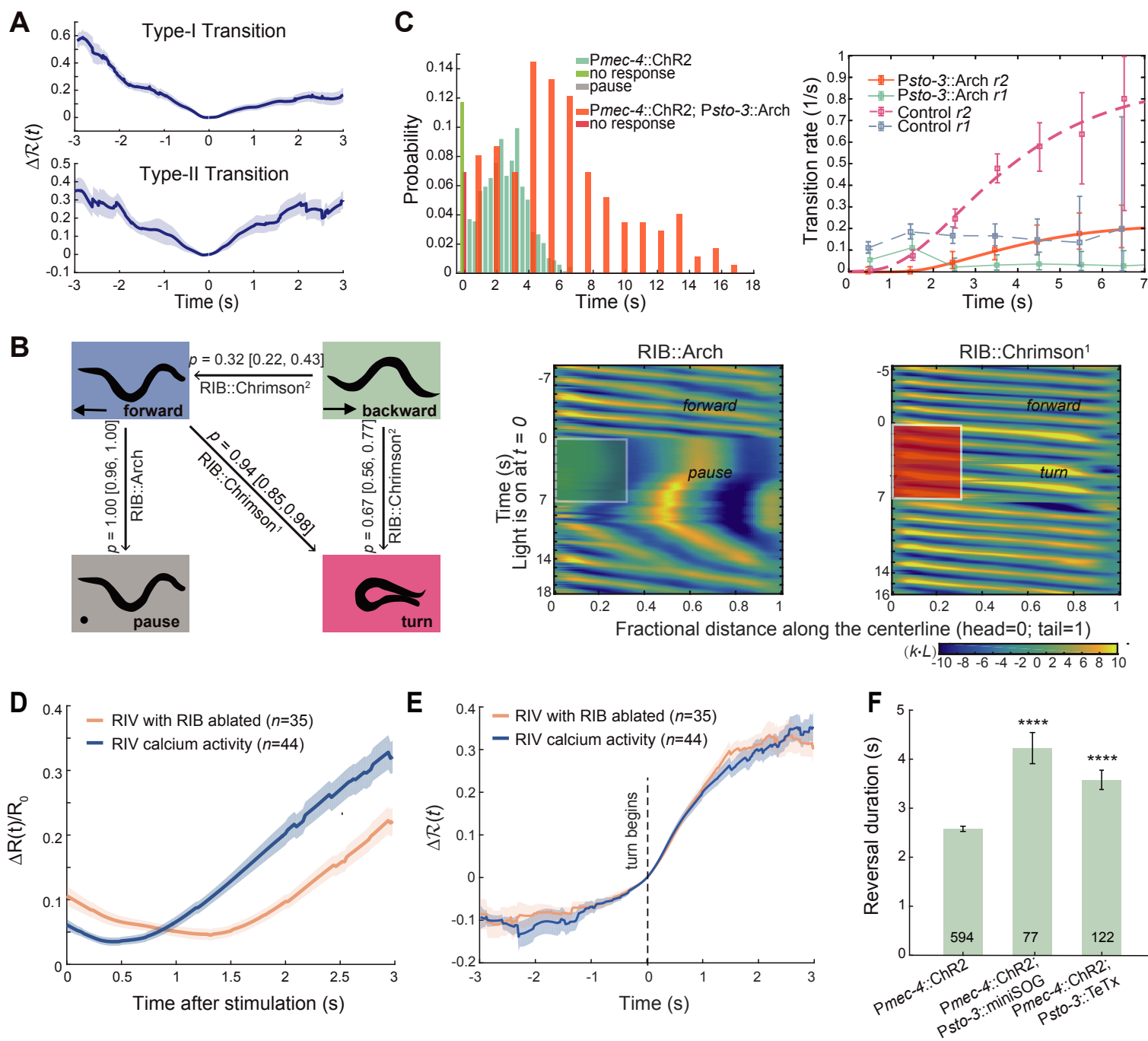
1190

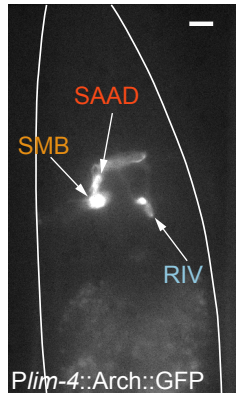
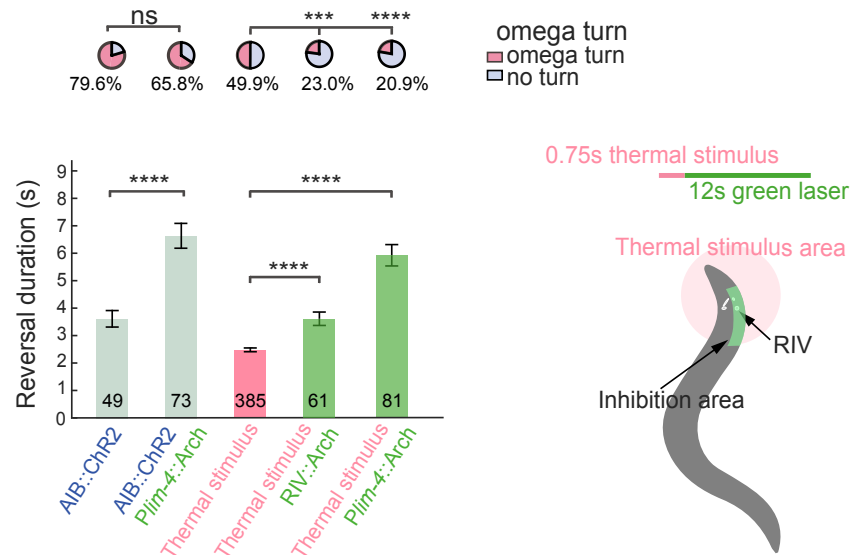
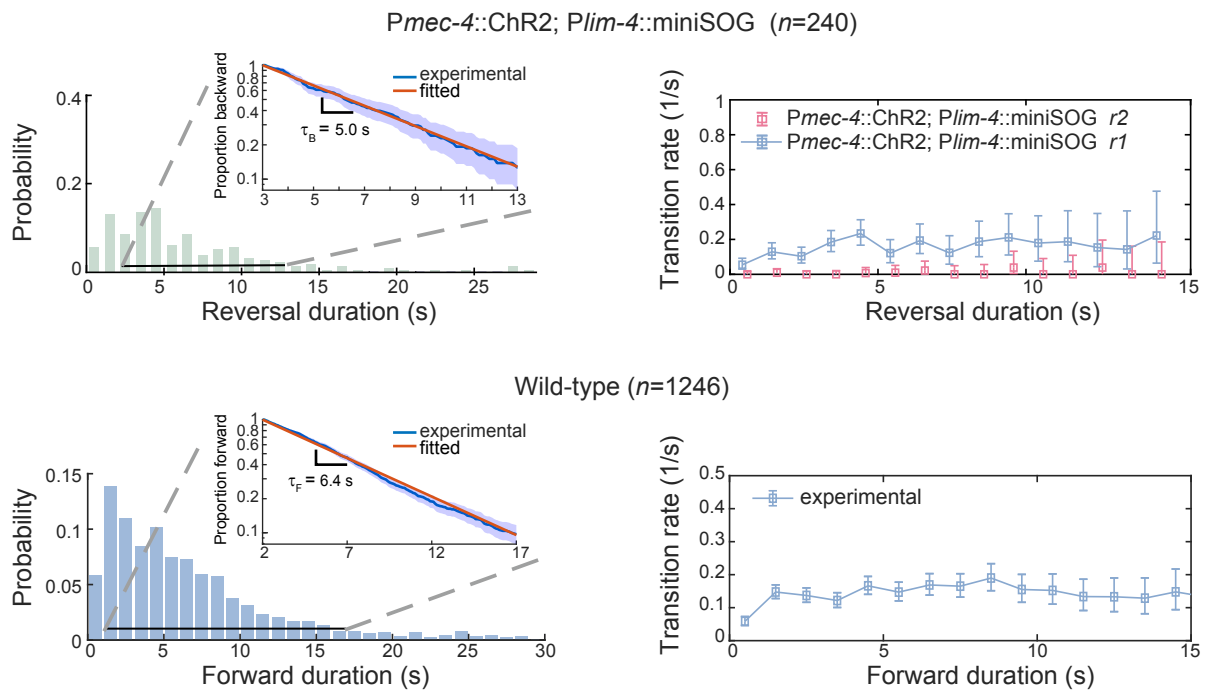
A**C****D****B**

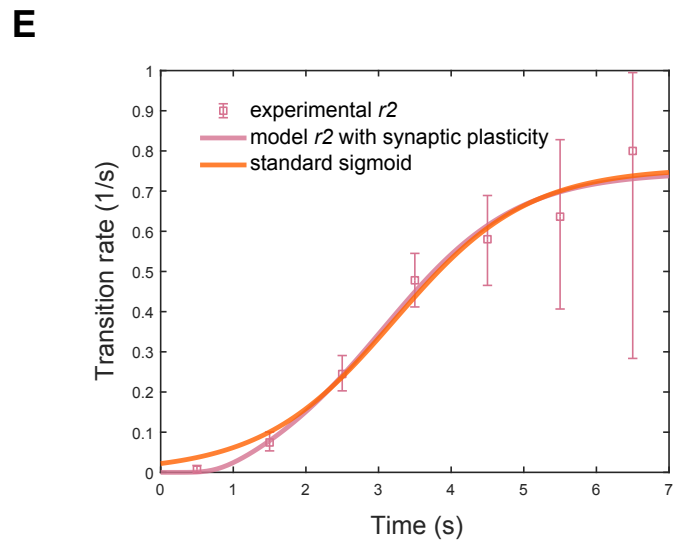
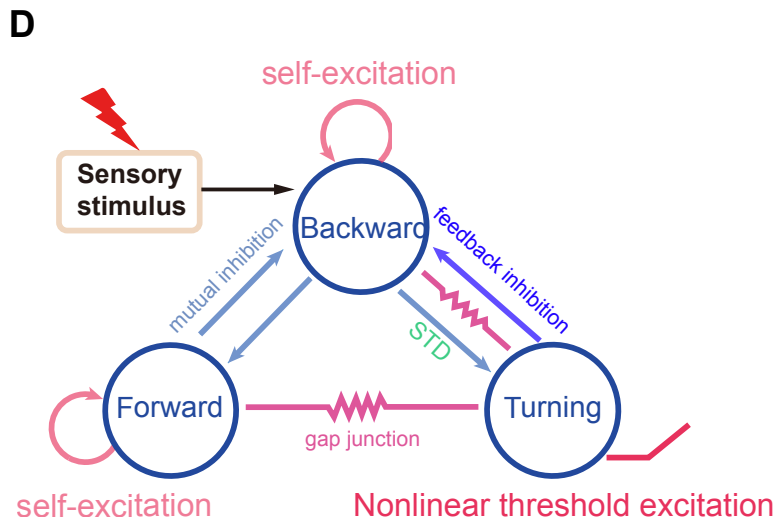
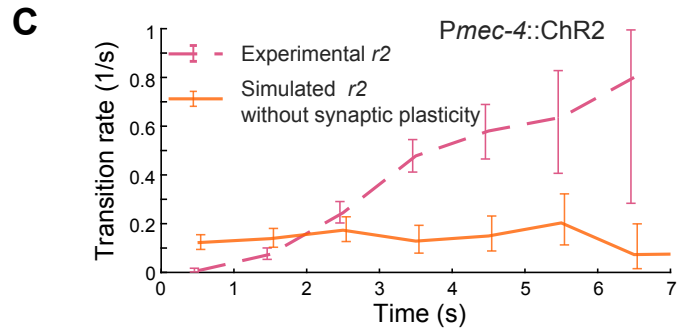
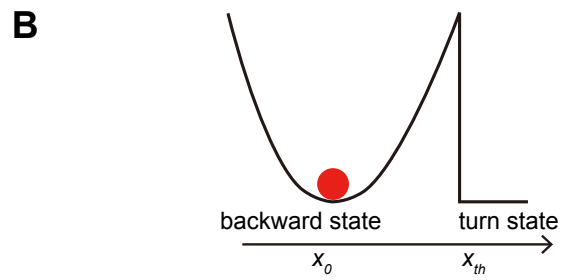
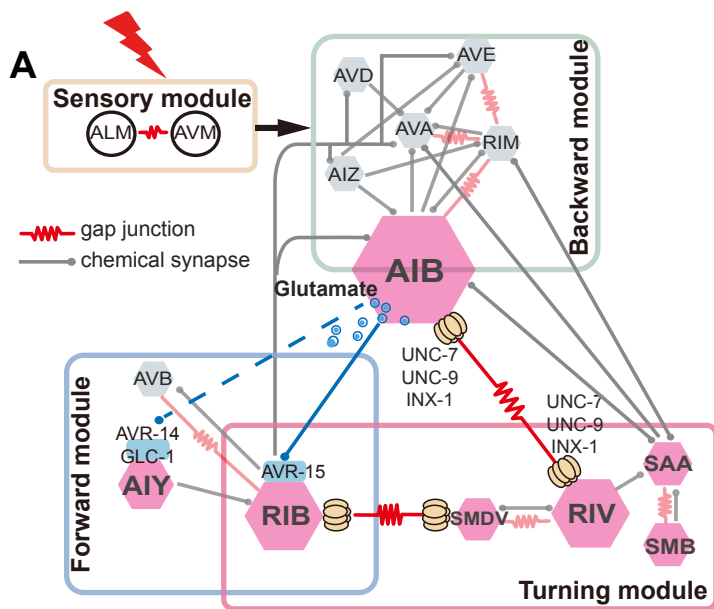


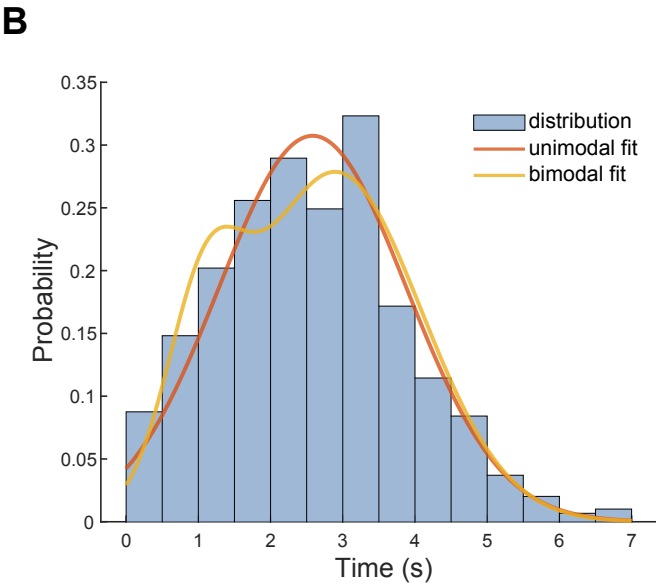
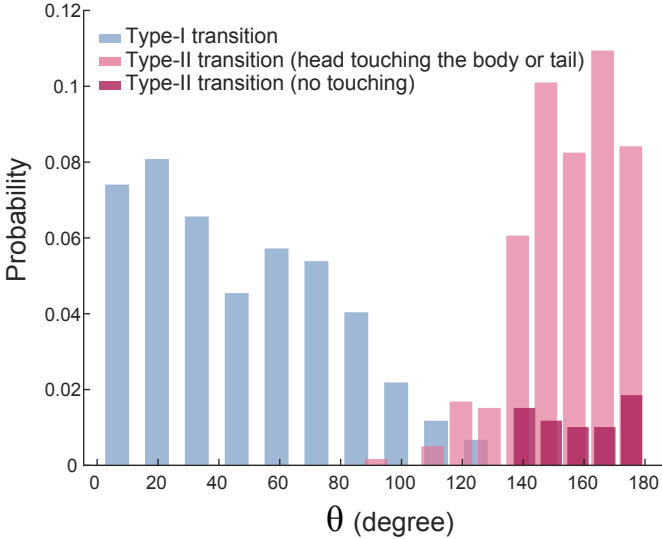
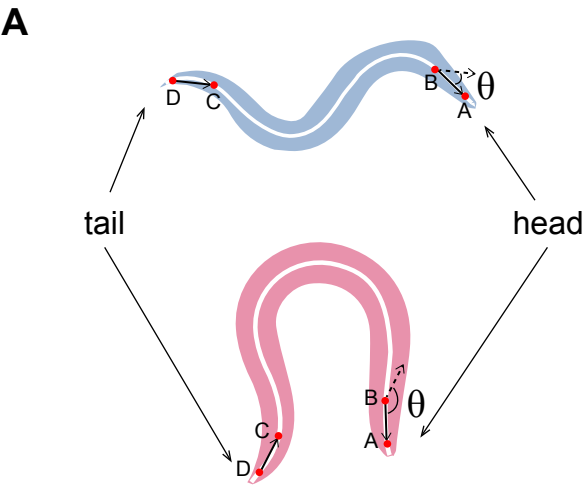




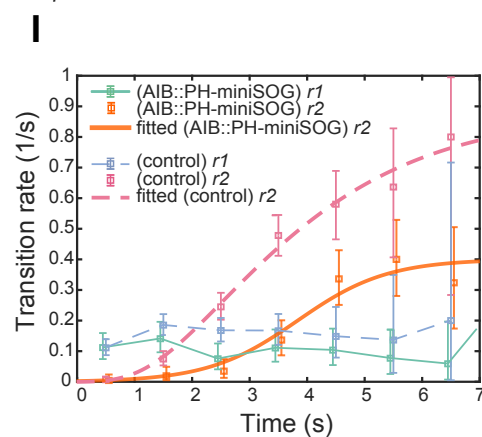
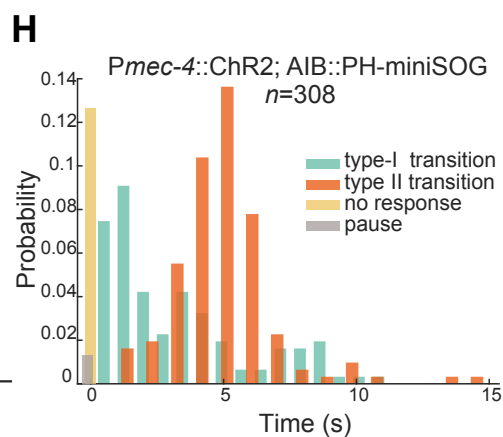
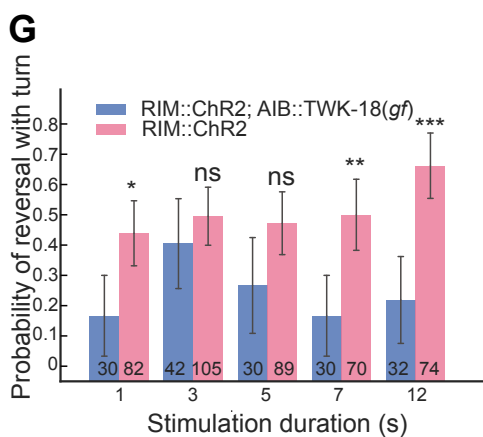
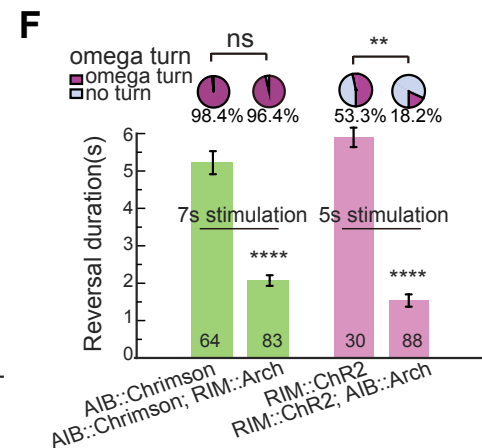
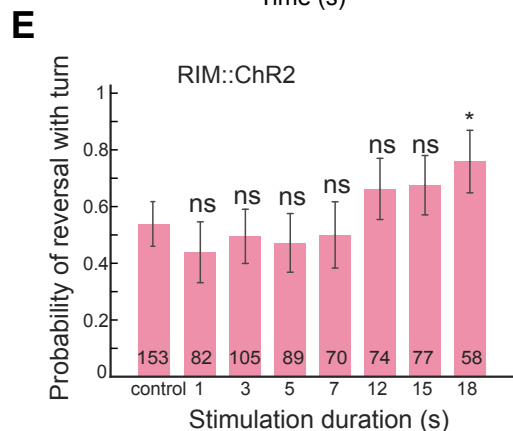
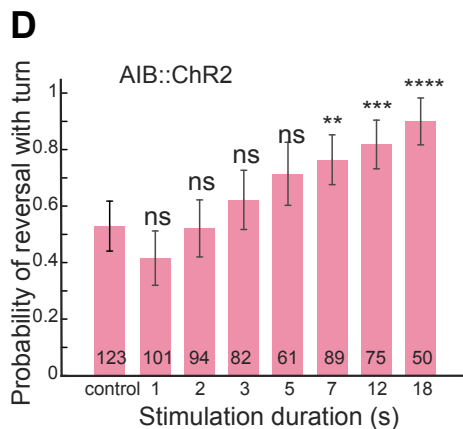
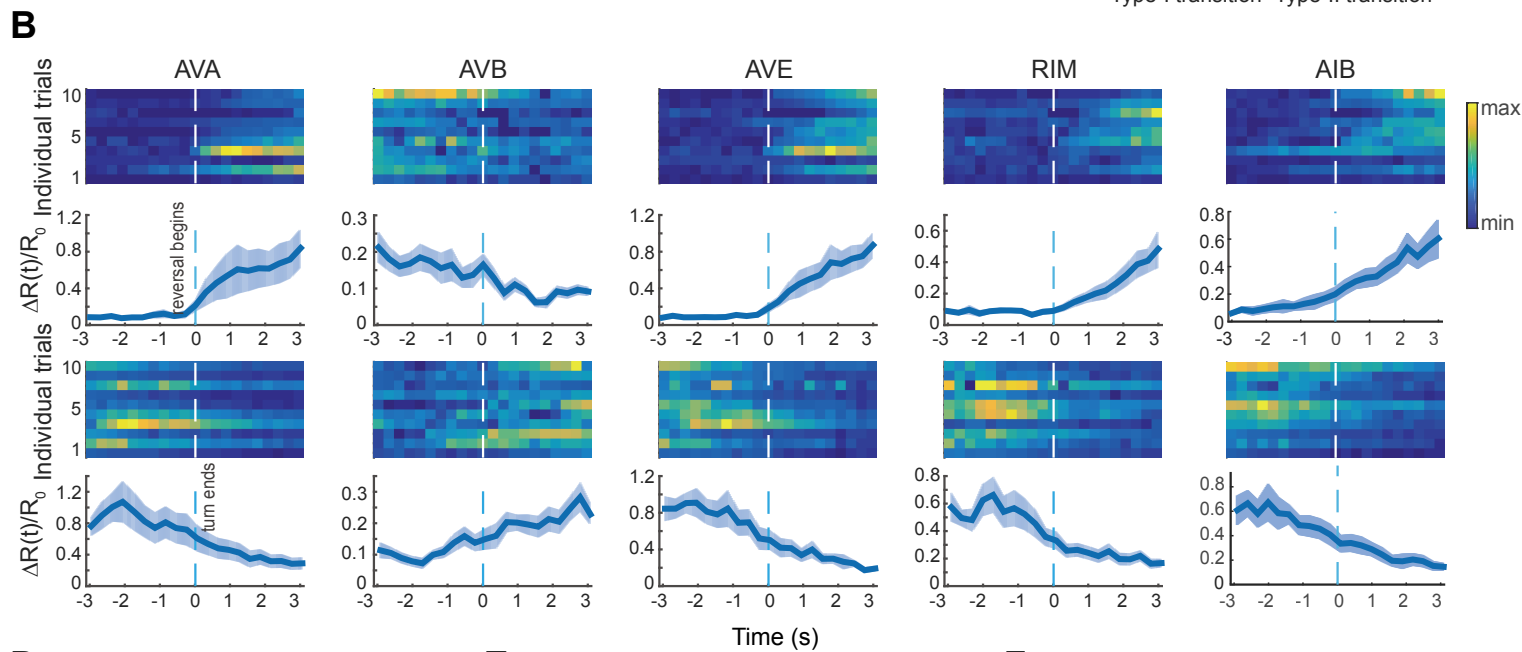
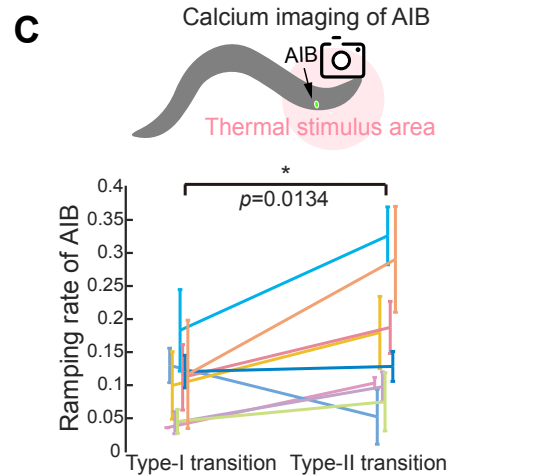
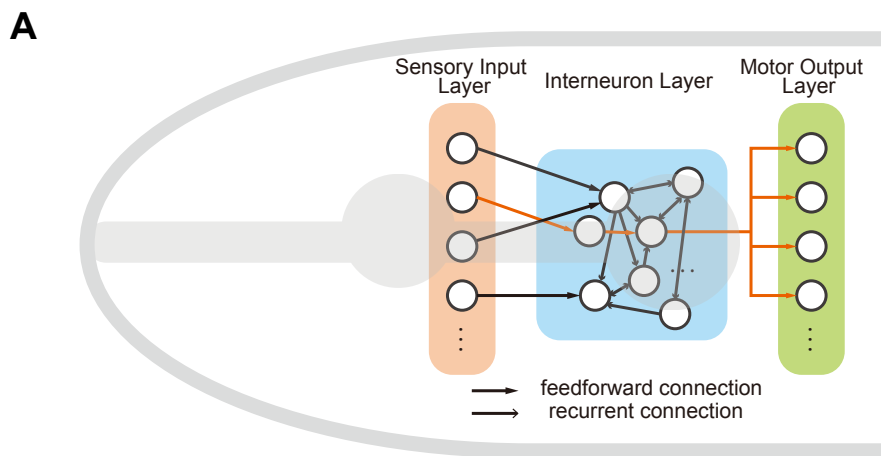


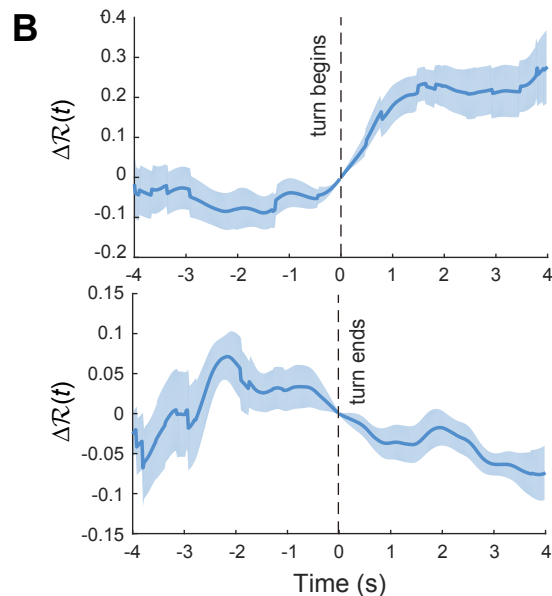
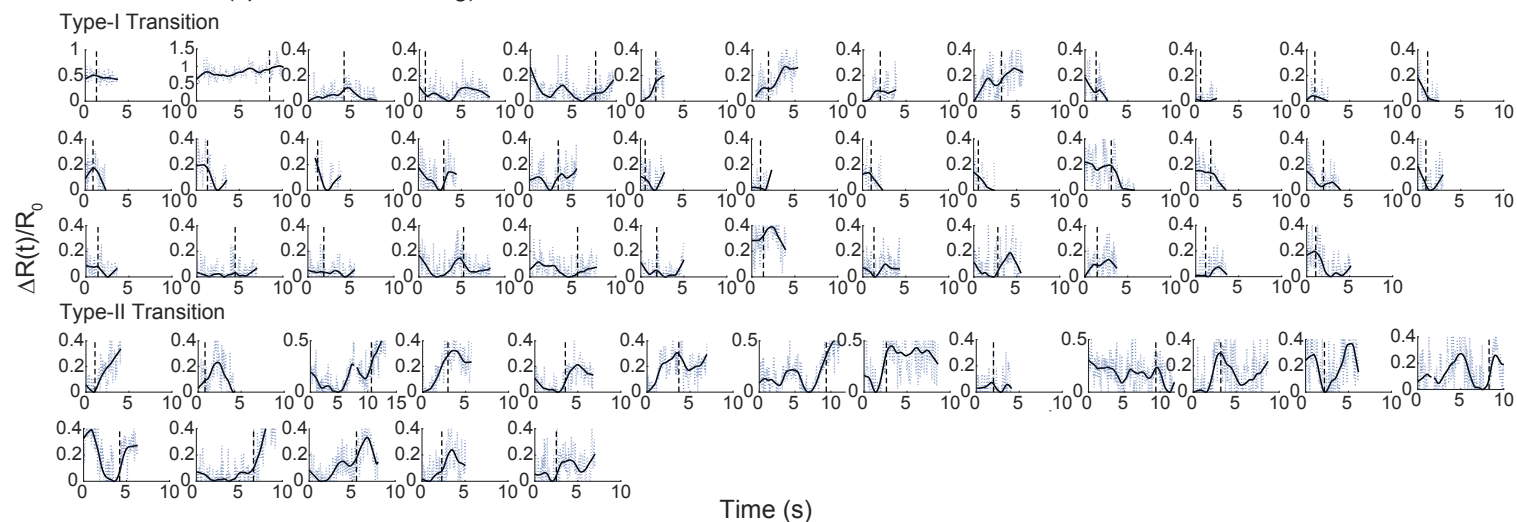
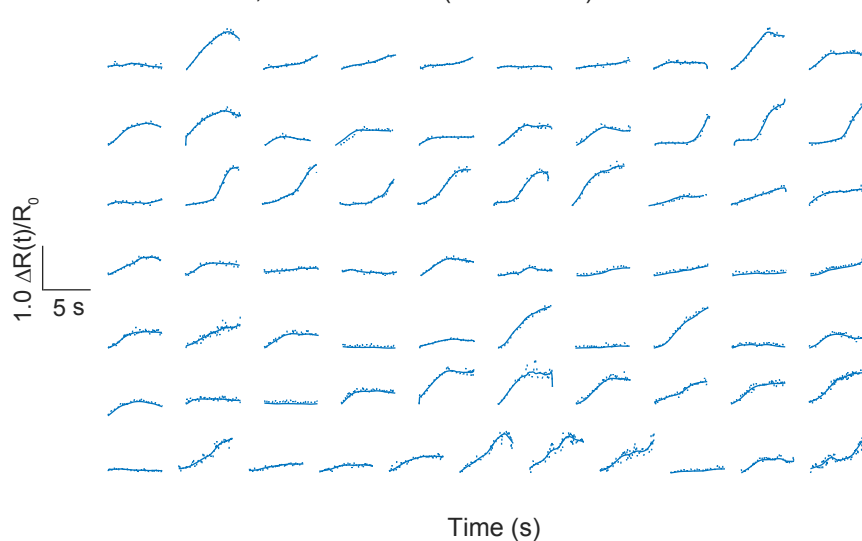
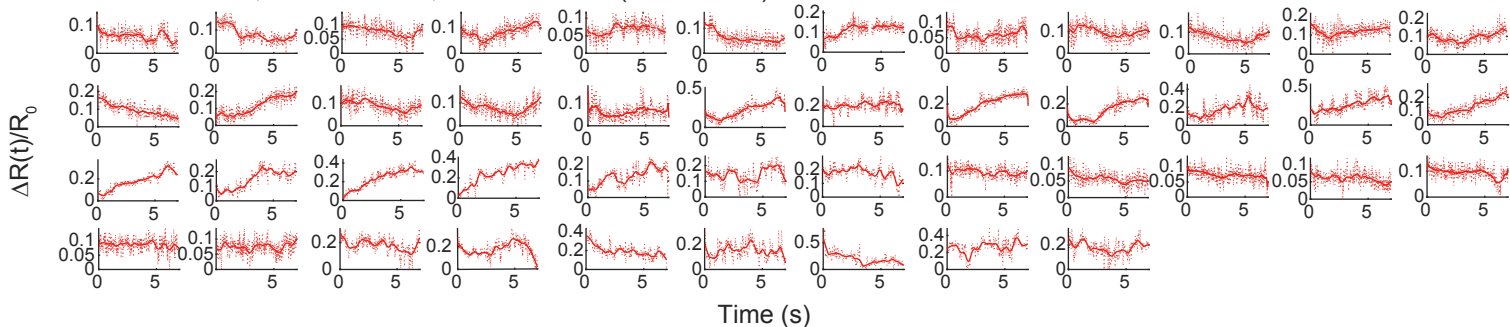
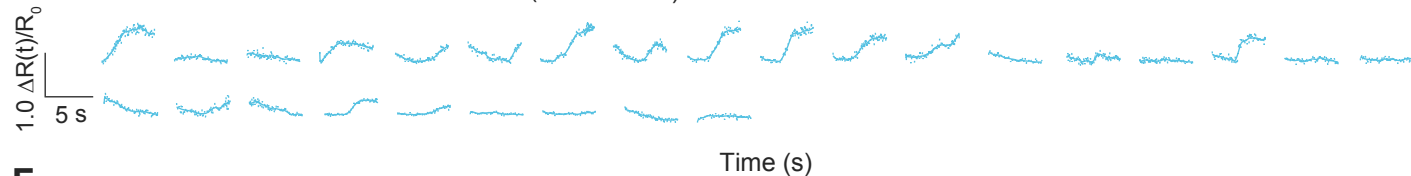
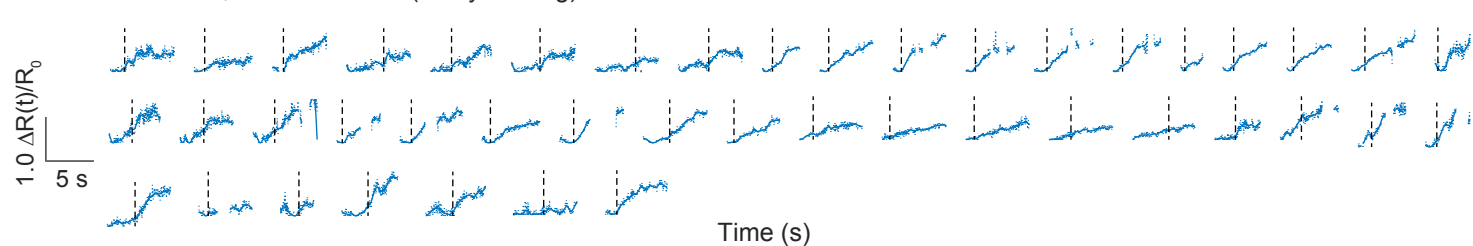
A**B****C**

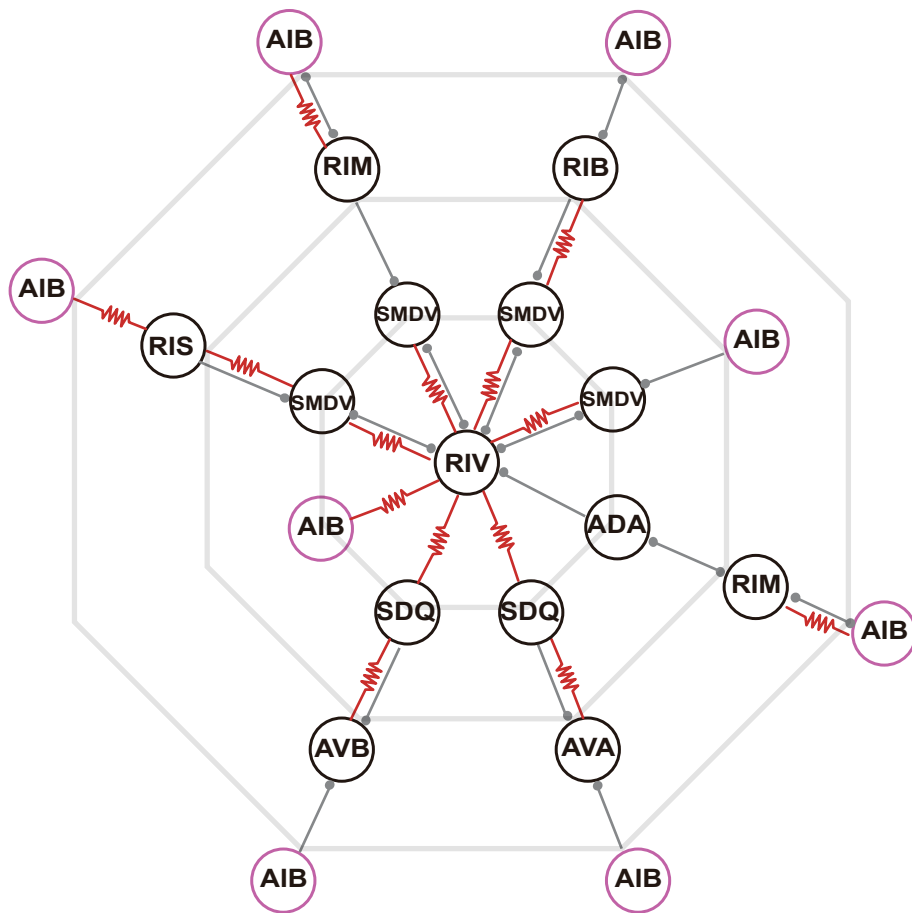




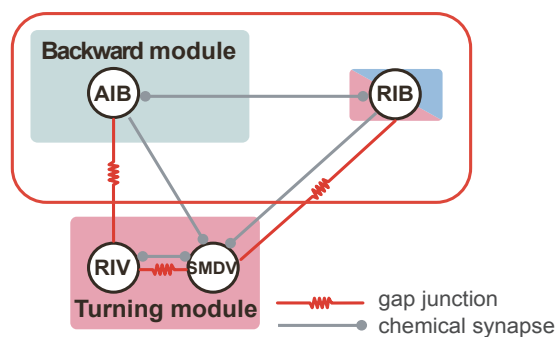
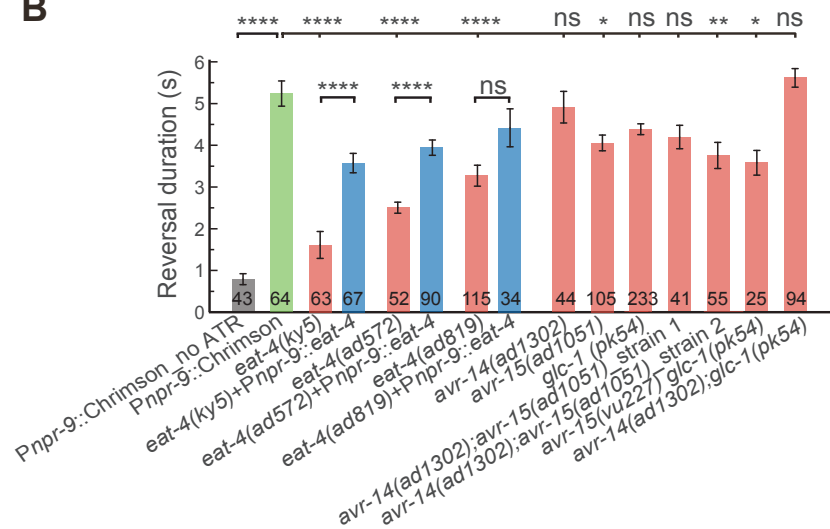
Model	Unimodal	Bimodal
Negative log likelihood	997.23	986.02
P-value	5.3435e-05	



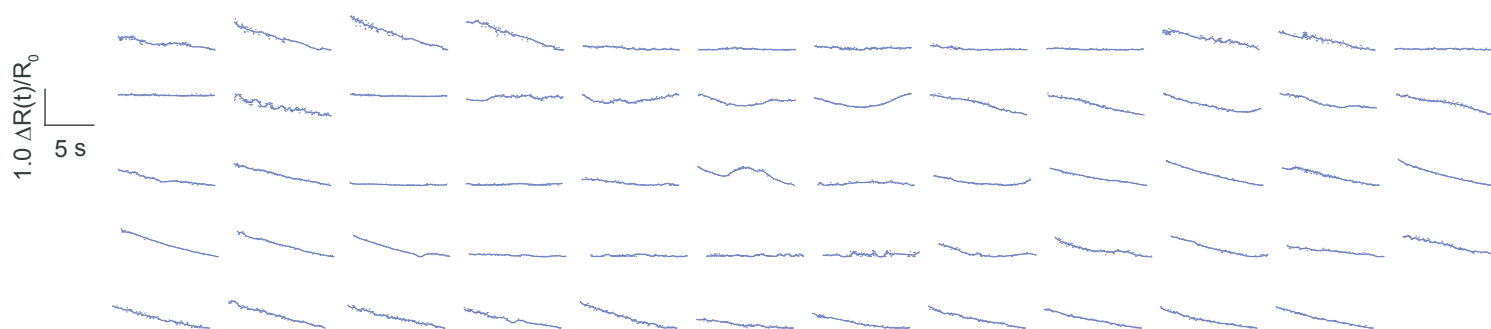
A RIV::GCaMP6 (spontaneous moving)**C** AIB::Chrimson; RIV::GCaMP6 (immobilized)**D** *inx-1 unc-7 unc-9*; AIB::Chrimson; RIV::GCaMP6 (immobilized)**E** AIB::Chrimson; RIV::Arch; RIV::GCaMP6 (immobilized)**F** AIB::Chrimson; RIV::GCaMP6 (freely moving)



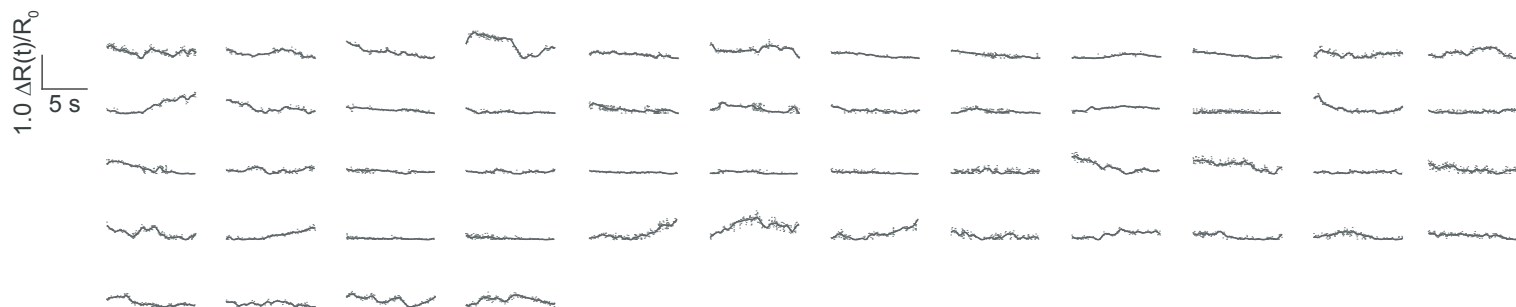
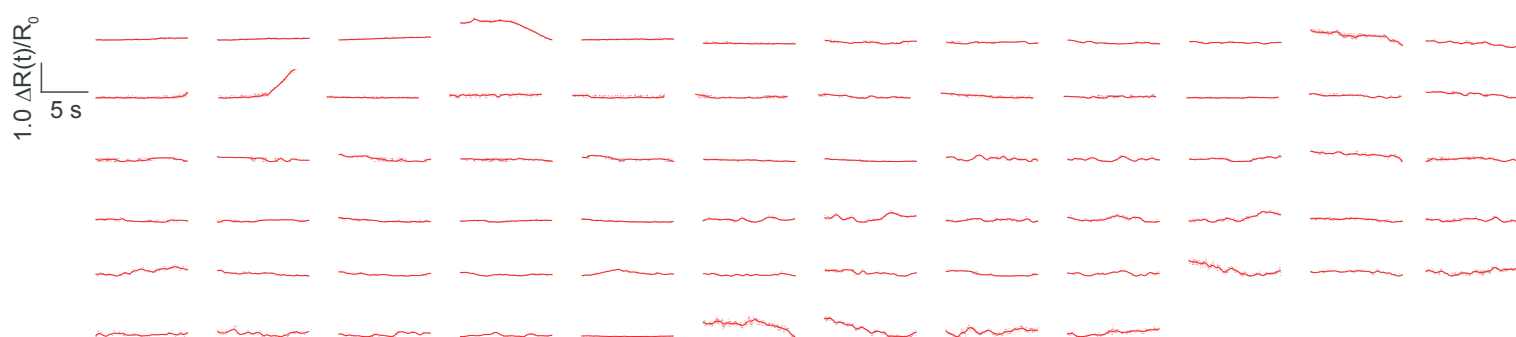
— gap junction
— chemical synapse

A**B****C**

AIB::Chrimson; RIB::GCaMP6 (control (ATR))

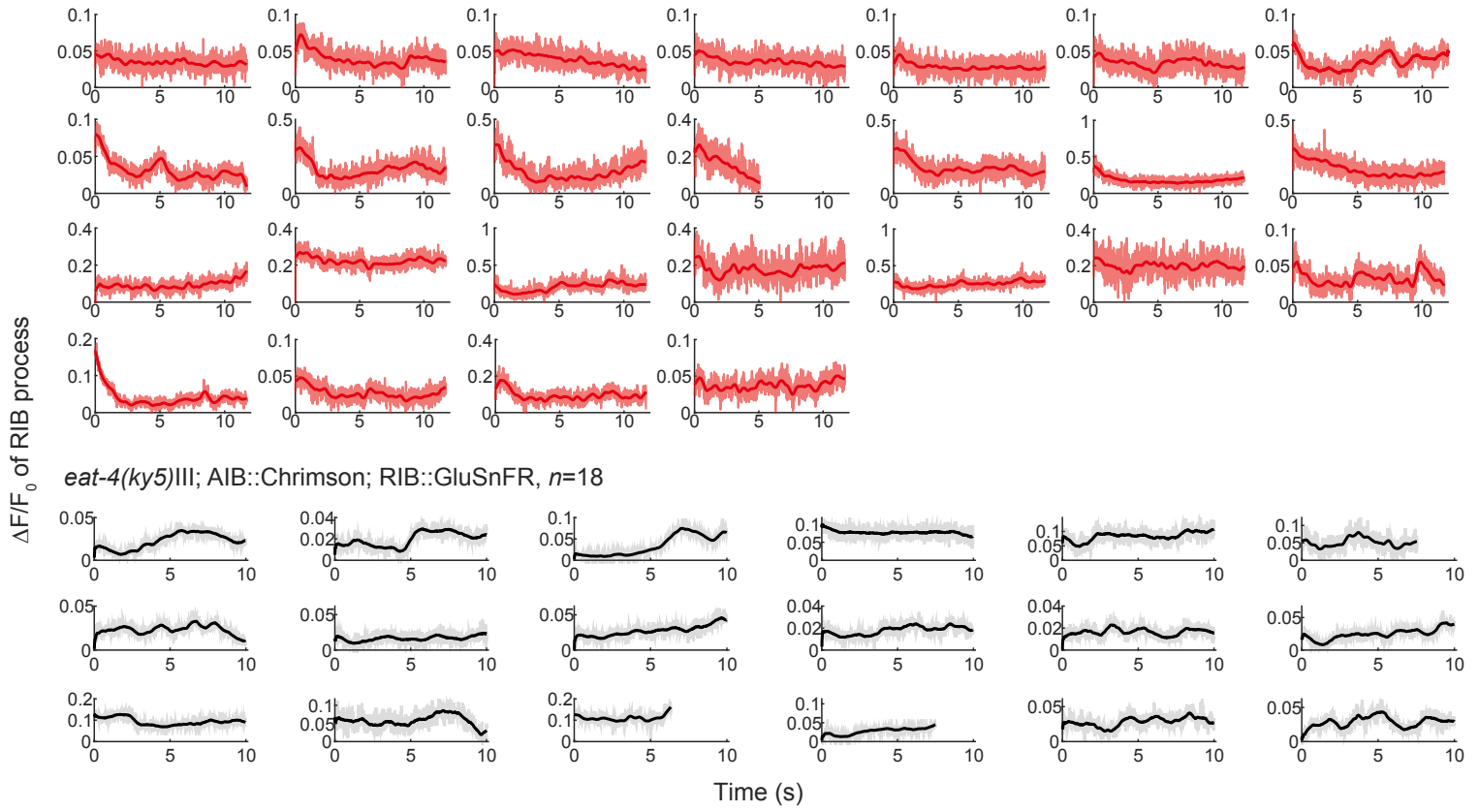


AIB::Chrimson; RIB::GCaMP6 (control (no ATR))

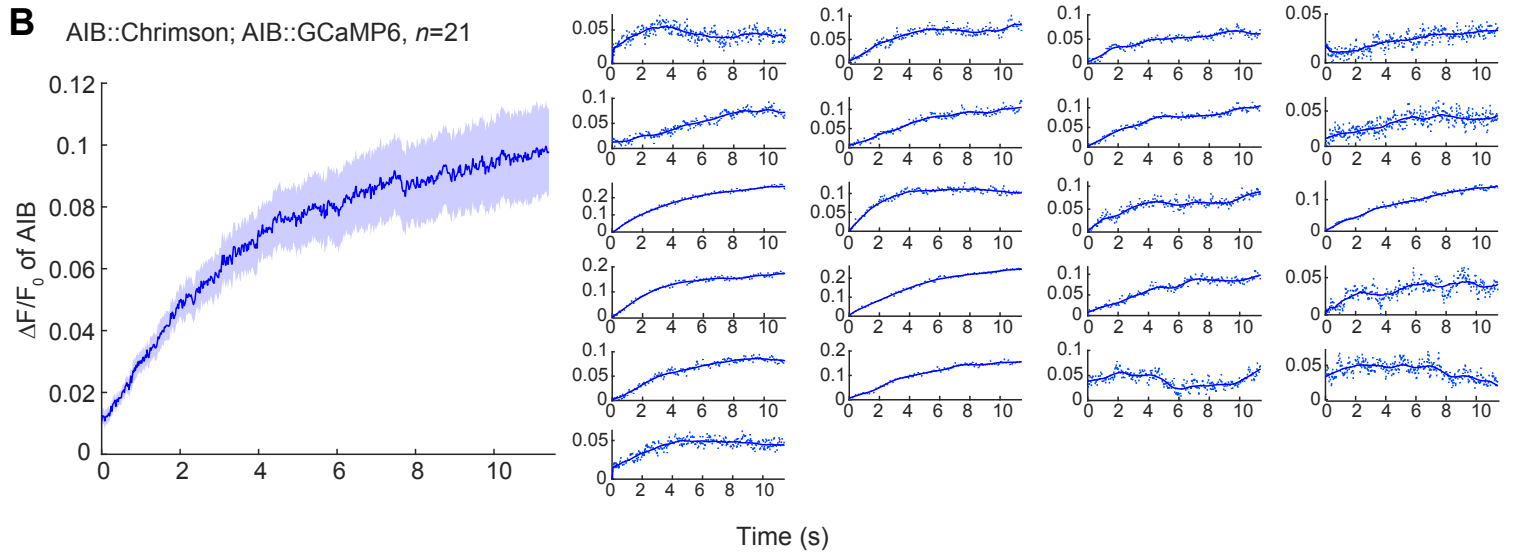
*eat-4(ky5)III*; AIB::Chrimson; RIB::GCaMP6

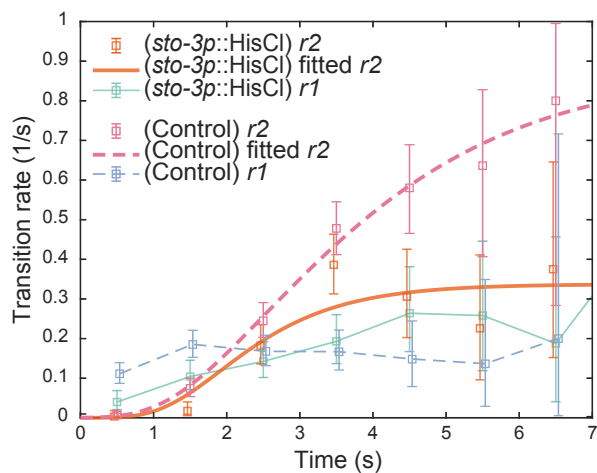
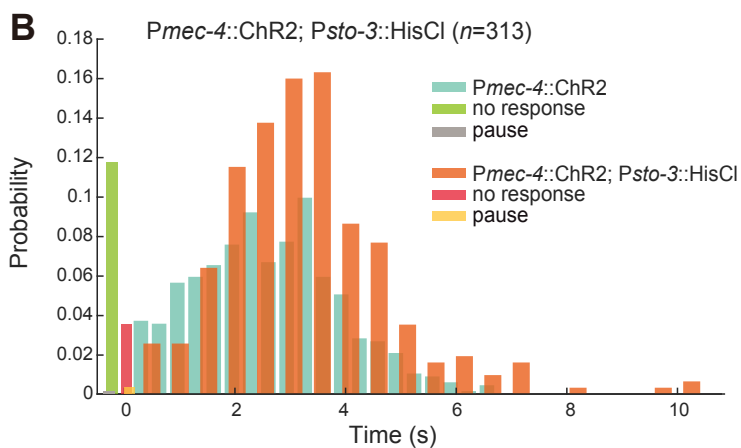
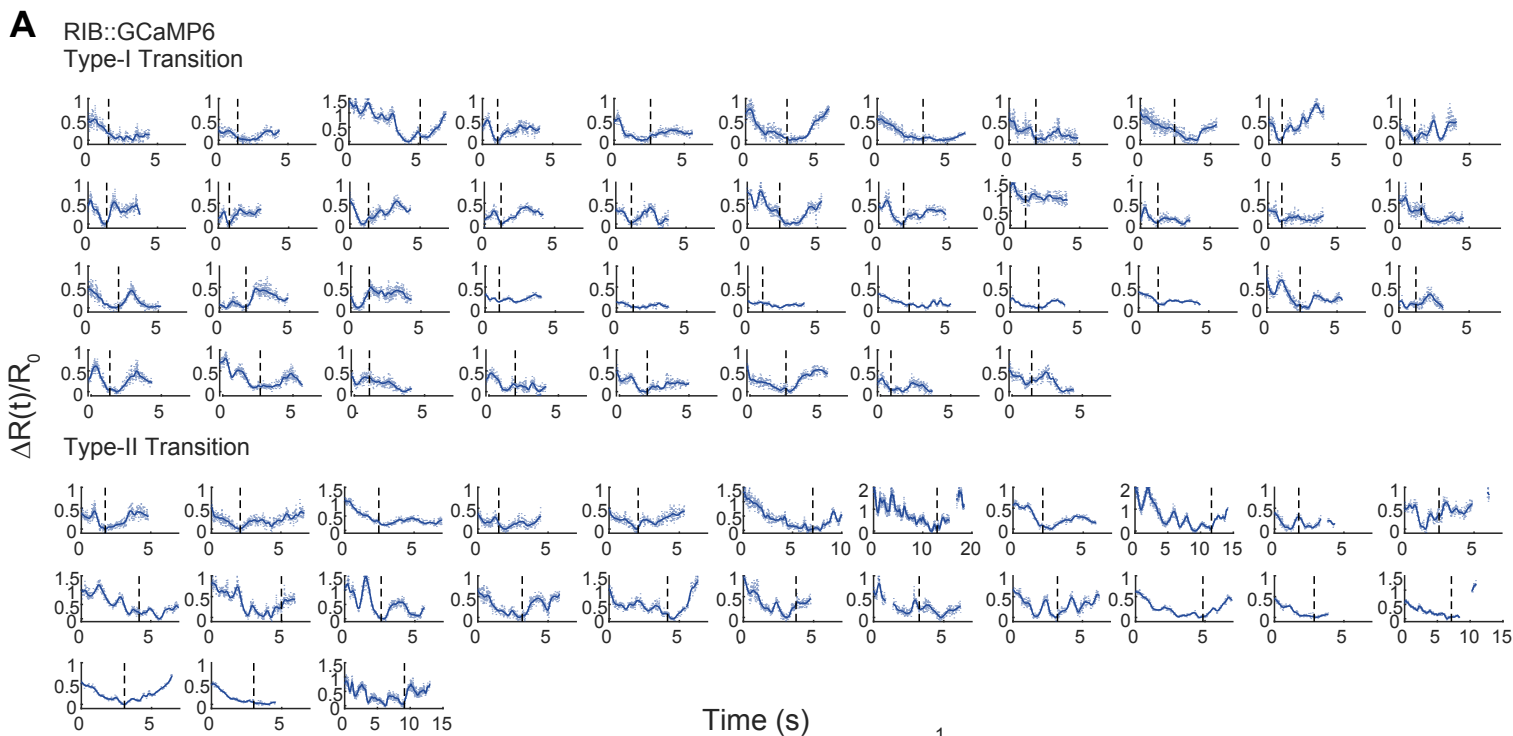
Time (s)

A AIB::Chrimson; RIB::GluSnFR, $n=25$

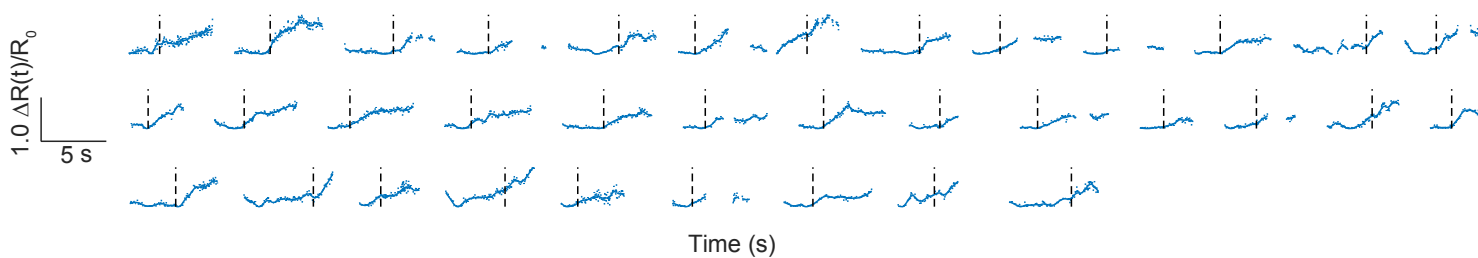


B AIB::Chrimson; AIB::GCaMP6, $n=21$





C AIB::Chrimson; *Plim-4::GCaMP6*; RIB::miniSOG (freely moving)



D AIB::Chrimson; *Plim-4::GCaMP6* (freely moving)

